The lead-glass electromagnetic calorimeters for the magnetic spectrometers in Hall C at Jefferson Lab

H. Mkrtchyan,[1] R. Carlini,[2] V. Tadevosyan,[1] J. Arrington,[3] A. Asaturyan,[1] M. E. Christy,[4] D. Dutta,[5]
R. Ent,[2] H. C. Fenker,[2] D. Gaskell,[2] T. Horn,[6] M. K. Jones,[2] C. E. Keppel,[4] D. J. Mack,[2] S. P. Malace,[5]
A. Mkrtchyan,[1] M. I. Niculescu,[7] J. Seely,[8] V. Tvaskis,[4] S. A. Wood,[2] and S. Zhamkochyan[1]

[1] *A. I. Alikhanyan National Science Laboratory (Yerevan Physics Institute), Yerevan 0036, Armenia*
[2] *Thomas Jefferson National Accelerator Facility, Newport News, Virginia 23606, USA*
[3] *Physics Division, Argonne National Laboratory, Argonne, Illinois 60439, USA*
[4] *Hampton University, Hampton, Virginia 23668, USA*
[5] *Triangle Universities Nuclear Laboratory and Duke University, Durham, North Carolina 27708, USA*
[6] *Catholic University of America, Washington, DC 20064*
[7] *James Madison University, Harrisonburg, Virginia 22807, USA*
[8] *Laboratory for Nuclear Science. Massachusetts Institute of Technology, Cambridge, MA, USA*
(Dated: May 1, 2012)

The electromagnetic calorimeters of the various magnetic spectrometers in Hall C at Jefferson Lab are presented. For the existing HMS and SOS spectrometers design considerations, relevant construction information, and comparisons of simulated and experimental results are included. The energy resolution of the HMS and SOS calorimeters is better than $\sigma/E \sim 6\%/\sqrt{E}$, and pion/electron ($\pi/e$) separation of about 100:1 has been achieved in energy range $1 - 5$ GeV. Good agreement has been observed between the experimental and simulated energy resolutions, but simulations systematically exceed experimentally determined π^- suppression factors by close to a factor of two. For the SHMS spectrometer presently under construction details on the design and accompanying GEANT4 simulation efforts are given. The anticipated performance of the new calorimeter is predicted over the full momentum range of the SHMS. Good electron/hadron separation is anticipated by combining the energy deposited in an initial (preshower) calorimeter layer with the total energy deposited in the calorimeter.

Keywords: electromagnetic calorimeter, pion/electron separation, electron detection efficiency, pion suppression factor, lead glass, photomultiplier.

I. INTRODUCTION

The experimental program at Jefferson Lab focuses on the studies of the electromagnetic structure of nucleons and nuclei, in particular in a region where a transition is expected from a nucleon-meson description into a quark-gluon description of matter. In experimental Hall C the emphasis has been on inclusive (e,e') electron scattering and proton knockout (e,e'p) experiments at the highest four-momentum transfer (Q^2) accessible, deuteron photodisintegration experiments, and both exclusive and semi-inclusive pion electroproduction reactions. In particular, the Hall C experimental program has studied the onset of the quark-parton model description of such reactions. To accomplish such a diverse program, a highly flexible set of instruments capable of accurate measurements of final momenta and angles is required, including both efficient background rejection and good particle identification properties. This remains very much in place after the 12-GeV Upgrade of Jefferson Lab (JLab) has been completed, with Hall C emphasizing precision measurements at high luminosities, with detection of high-energy reaction products approaching the beam energy at very forward angles.

The initial base equipment of Hall C was well suited to the JLab scientific program that required high luminosity, intermediate detector acceptances and resolution [1]. With the high luminosities needed to access neutrino-like

scattering probabilities comes a high-background suppression requirement. The magnetic spectrometer pair that constituted the base equipment pointed to a common pivot with scattering chamber. The Short Orbit Spectrometer (SOS), with a QD$\bar{\text{D}}$ configuration, accessed a momentum range of 0.3 - 1.7 GeV/c, and an angular range of 13.3° - 168.4°. It was explicitly designed to measure pions and kaons with short life times. The High Momentum Spectrometer (HMS), with a QQQD magnetic configuration, covered a momentum range 0.5 - 7.3 GeV/c, but was to date not used above 5.7 GeV/c. The HMS accessed an angular range between 10.5° - 80°.

After the JLab 12-GeV Upgrade [2], the Hall C scientific program is again focused on high luminosity measurements with detection of high energy reaction products at small forward angles. Such a physics program can be accessed only by a spectrometer system providing high acceptance for, given the larger boosts associated with the energy upgrade, very forward-going particles, and analyzing power for particle momenta approaching that of the incoming beam. To accomplish this, and maintain a spectrometer pair rotating around a common pivot for precision coincidence measurements, the SOS will be superseded by the newly built Super High Momentum Spectrometer (SHMS). The SHMS will achieve a minimum (maximum) scattering angle of 5.5° (40°) with acceptable solid angle and do so at high luminosity. The maximum momentum will be 11 GeV/c, well matched

TABLE I: The basic parameters of the HMS, SOS and SHMS spectrometers.

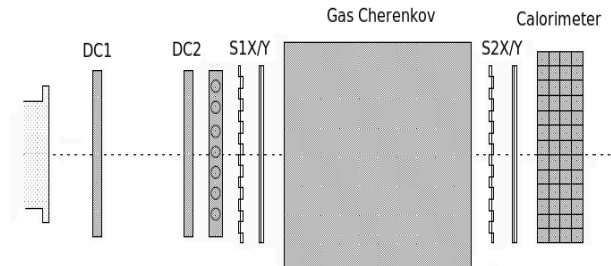| Parameter	HMS	SOS	SHMS
Momentum Range (GeV/c)	0.5-7.3	0.3-1.7	1.5-11.0
Momentum Acceptance (%)	±10	±20	-10 - +22
Momentum resolution (%)	0.10-0.15	<0.1	0.03-0.08
Horiz. Angl. Accept.(mrad)	±32	±40	±18
Vert. Angl. Accept. (mrad)	±85	±70	±50
Solid angle (msr)	8.1	9.0	> 4.5
Maximum scattering angle	$\leq 80^o$	$\leq 168.4^o$	$\leq 40^o$
Minimum scattering angle	$\geq 10.5^o$	$\geq 13.3^o$	$\geq 5.5^o$
Horiz. Angl. res. (mrad)	0.8	0.5	0.5-1.2
Vertical Angl. res. (mrad)	1.0	1.0	0.3-1.1
Vertex Reconstr. res. (cm)	0.3	2-3	0.1-0.3

FIG. 1: Schematic side-view of the HMS detector package. The aerogel detector was added between the DC2 drift chamber and the S1X hodoscope in 2003. Adapted from [22].

to the maximum energy available in Hall C. The basic parameters of the HMS, SOS and SHMS are listed in Table I.

The standard detector packages in the HMS and SOS were designed from inception to be very similar [22]. The detector stacks, shown for the HMS in Fig. 1, are located inside the respective concrete spectrometer shield houses. A pair of six-plane drift chambers (DC1 and DC2) is situated immediately after the dipole magnet, in the forefront of shield house to allow for particle tracking. They are followed by two pairs of x-y scintillator hodoscopes sandwiching a gas Čerenkov. In some experiments, an aerogel Čerenkov detector was added either before (HMS) or after (SOS) the pairs of scintillators. The last detector in the detection stack is the lead-glass electromagnetic calorimeter, positioned at the very back of the shield house. Its support structure is in fact mounted on the concrete wall of the shield house. The two sets of drift chambers are used for track reconstruction, the four scintillating hodoscope arrays for triggering and time-of-flight measurements, and the threshold gas (and aerogel) Čerenkov detectors and lead-glass calorimeters for electron/hadron separation.

Hall C experiments typically demand well-understood detection efficiencies of better than 99%, and background particle suppression of 1,000:1 in e/π separation, typically. This can be achieved by combining 100:1 suppression in the electromagnetic calorimeter, with the remaining suppression in a gas Čerenkov counter. Several experiments used signals from the calorimeter and gas Čerenkov counters already in a hardware trigger to reject pions or electrons by a factor of 25:1 in the online data acquisition system. The Particle Identification (PID) systems of both spectrometers performed remarkably stable over more than a decade of use. The combination of gas Čerenkov and lead-glass electromagnetic calorimeter ensured pion suppressions of typically a few 1,000:1, for electron detection efficiency of better than 98%.

The detector package of the SHMS will be a near-clone of the HMS. It will again include a pair of multiwire drift chambers for tracking, and scintillator and quartz hodoscopes for timing. As the SHMS will both detect a variety of hadrons (π, K, p) in a number of coincidence experiments with HMS, and electrons in single-arm (e,e′) experiments, special attention is again paid to the PID system. It must provide similar particle identification as mentioned above, even at the higher energies. In its basic configuration the SHMS detection stack includes a heavy gas Čerenkov for hadron selection, and a noble-gas Čerenkov and lead-glass electromagnetic calorimeter for electron/hadron separation. It is again envisaged to augment the detector stack with aerogel Čerenkov detectors, primarily for kaon identification. The approved experiments demand a suppression of pion background for electron/hadron separation of 1,000:1, with suppression in the electromagnetic calorimeter alone on the level of 100:1. An experiment to measure the pion form factor at the highest Q^2 accessible at JLab with 11 GeV beam [3] requires a strong suppression of electrons against negative pions of a few 1,000:1, with a requirement on the electromagnetic calorimeter of a 200:1 suppression.

This paper describes the electromagnetic calorimeters in the various magnetic spectrometers, be it existing or under construction, in Hall C at Jefferson Lab. Section II describes in detail the pre-assembly studies, the component selection, construction and assembly of the HMS and SOS calorimeters. Section III explains the Monte Carlo simulation package used, and highlights the structure and some details of the simulation software. Sections IV and V cover the electronics and calibration of the calorimeters. We present resolution, efficiency and hadron rejection capability of the calorimeters in both HMS and SOS, and compare experimental data with simulation results. In Section VI we describe details of the newly designed calorimeter for the SHMS, including information on the component selection and construction. We also present results of pre-assembly component checkout, and the anticipated performance of the SHMS calorimeter from simulation studies.

II. HMS AND SOS CALORIMETERS

Particle detection using electromagnetic calorimeters is based on the production of electromagnetic showers in a material. The total amount of the light radiated in this case is proportional to the energy of the primary particle. Electrons (as well as positrons and photons), will deposit their entire energy in the calorimeter giving a detected energy fraction of one. The energy fraction is the ratio of energy detected in the calorimeter to particle energy.

Charged hadrons entering a calorimeter have a low probability to interact and produce a shower, and may pass through without interaction. In this case they will deposit a constant amount of energy in the calorimeter. However, they may undergo nuclear interactions in the lead-glass and produce particle showers similar to the electron and positron induced particle showers. Hadrons that interact inelastically near the front surface of the calorimeter and transfer a sufficiently large fraction of their energy to neutral pions will mimic electrons. The maximum attainable electron/hadron rejection factor is limited mainly by the cross section of such interactions.

A. Construction

R&D, design and construction of the calorimeters for the HMS and SOS magnetic spectrometers started in 1991-1992. In 1994 both calorimeters were assembled and installed as part of the instrumentation of Hall C spectrometers, becoming the first operational detectors at JLab. Since the first commissioning experiment, the calorimeters have been successfully used in nearly all experiments carried out in Hall C. In 2008, the SOS spectrometer was retired and its calorimeter blocks removed to be used for the preshower of the newly designed SHMS spectrometer. The HMS calorimeter will remain in place for use after the Continuous Electron Beam Accelerator Facility's (CEBAF) 12–GeV upgrade.

The HMS/SOS calorimeters are of identical design and construction except for their total size. Blocks in each calorimeter are arranged in four planes and stacked 13 and 11 blocks high in the HMS (see Fig. 2) and SOS respectively. The planes are shifted relative to each other in the vertical direction by ~5 mm. In addition, the entire detector is tilted by 5° relative to the central ray of the spectrometer. These shifts make it impossible for particles to pass through the calorimeter without interaction. The total thickness of the material along the particle direction of ~14.6 radiation lengths is enough to absorb the major part of energy of electrons within the HMS momentum range.

All blocks were produced in early 1990's by a Russian factory in Lytkarino [4], whose products of good optical quality were well known. The blocks are 10 cm × 10 cm × 70 cm in size and machined with a precision of 0.05 mm. They may contain bubbles or stones with a diameter less than 300 μm with an impurity frequency of less than 5-10
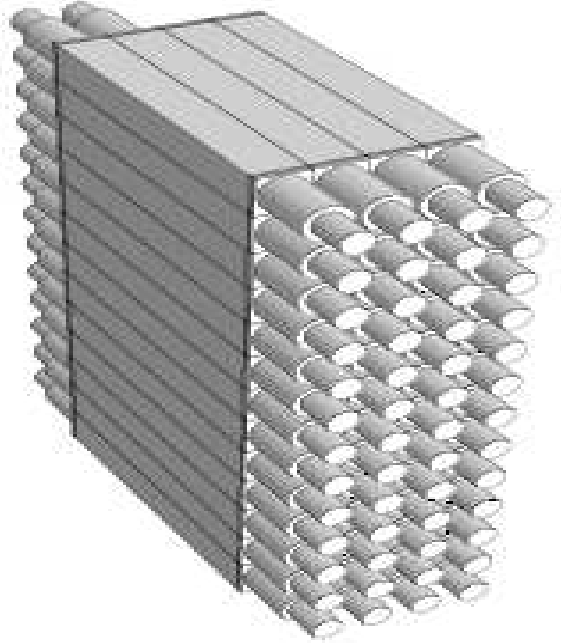

FIG. 2: A sketch of the HMS calorimeter. The front of detector is at left. The left side PMTs were added in 1998.

per kg of glass.

The optics and acceptances of the spectrometers (see Table I) required the calorimeters to have frontal dimensions about 60×120 cm^2 for the HMS and 60×100 cm^2 for the SOS. To avoid any shower leakage from the calorimeter volume, we chose to extend the physical dimensions of the calorimeters at least 5 cm beyond the sizes required by spectrometer acceptance. This gave calorimeter physical areas of 70×130 cm^2 for the HMS and 70×110 cm^2 for the SOS.

Looking from the side, the HMS calorimeter consists of 52 modules stacked in 4 columns (each layer 3.65 rad. length thick) (see Fig. 2). In addition to total energy deposition of the particle, a modular calorimeter gives information on the longitudinal development of the shower (which is different for electromagnetic and hadronic showers). This additional information can be used for more effective electron/hadron selection. Since the modules are oriented transversely to the incident particles, to detect photons from Čerenkov radiation one needs to attach photomultipliers (PMTs) from the side of the block and cover the area 10×10 cm^2 of the blocks as effectively as possible. The energy resolution of a lead-glass shower counter depends strongly on the ratio of the photocathode area to the output area of the radiator [5]. Photomultipliers with a photocathode diameter of 3.0"-3.5" were considered to be the optimal choice for the HMS/SOS calorimeters since they could provide a relatively high value of ~0.44 - 0.50 for this ratio.
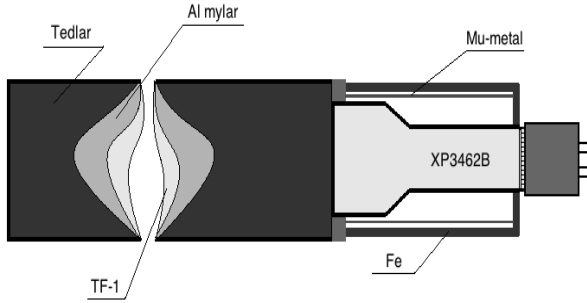
FIG. 3: Structure of the lead-glass module.

B. The single module assembly

The requirement that the lead glass blocks must be optically isolated and optically coupled to PMTs was the primary guidance for the construction. The individual module design is shown in Fig. 3. To ensure light-tightness, each block is wrapped in 25 μm thick aluminized Mylar and 40 μm thick Tedlar type film. There is a thin layer of air between the block and Mylar, for optical insulation was not completely tight wrapped. Each block is also equipped with ST type optical fiber adapter for light monitoring system. The blocks are slightly different in sizes, but on average the spread in length is less than ± 0.250 mm and less than ± 0.100 mm (100$\pm$0.10 mm) in transverse size. The gaps between the modules in final assembly are less than 250 μm.

The calorimeter signals from the blocks are read out by 8-stage Philips XP3462B photomultiplier tubes. The PMTs are shielded by six turns of 100 μm thick μ-metal foil. Since the PMTs operate at negative high voltage and the photocathodes are near the magnetic shields and other mechanical parts at ground potential, special protection is required to avoid current leakage between the photocathodes and ground. For this reason, the PMT bulbs were wrapped in several layers of thin Teflon and black electrical tape. After full assembly, the current leak for each block was measured with a high voltage about 200 V above nominal operating setting.

Silicone grease ND-703 with high viscosity is used for the PMT – block optical contact (index of refraction $\sim$1.46). Originally PMTs were attached to only right side of the blocks (looking along the central ray of the HMS). The PMTs on the left side in the first two layers were added in the late 1998 in order to enhance signal output, especially at low energies. In addition, this weakens dependence of the aggregate signal from a module on the particle's point of impact.

C. Photomultiplier tube selection and studies

The choice of the photomultiplier tube depends on the intensity of light to be measured and the regime of its operation. One of the most important requirements for the PMTs used in the HMS/SOS calorimeters was high efficiency for the electrons above $\sim$100 MeV, and good linearity up to the energies of several GeV. At low energy (or low light intensity) the PMT must have relatively high gain in order to keep electron trigger efficiency high. But, in all cases its operation regime must be optimized for best signal-to-noise ratio.

Ideally, the gain of a PMT with n dynode stages and an average secondary emission ratio δ per stage is $G \sim \delta^n$. While the secondary emission ratio is given by $\delta = A \cdot \triangle V^\alpha$, where A is a constant, $\triangle V \approx V/(n+1)$ is the interstage voltage, and α is a coefficient which depends on the dynode material and geometric structure (typically $\alpha \approx$0.7-0.8). For a voltage V applied between the cathode and the anode, the gain is roughly $G \approx k \cdot V^{\alpha n}$, where k is a constant. So the gain (or the PMT output signal amplitude) is proportional to the applied voltage V and will increase as $V^{\alpha n}$ (in the linearity range of the PMT).

But with the applied high voltage the anode dark current will also increase (current in the PMT even when it is not illuminated). Major sources of dark current are thermoelectric emission of electrons from the materials, ionization of residual gases, glass scintillation, leakage current from imperfect insulation. The resulting noise from the dark current is a critical factor in determining the low limit of light detection, in the optimization of the PMT gain (via high voltage), especially when the rate of dark current change varies.

The choice of XP3462B PMT was made after studies of several other 3 inch and 3.5 inch photomultiplier tubes on the matter of having good linearity, photocathode uniformity, high quantum efficiency, and good timing properties. Gain variations with HV and dark currents also were measured.

In order to understand the limits imposed by the PMTs on the performance of the detector, several tests were performed on a set of candidate PMTs [6]. All showed excellent linearity over a 3500:1 dynamic range of a reasonably chosen high voltage, as well as good time and amplitude resolutions. For pulses corresponding to photoelectron (pe) yield of $N_{pe} = 10^3$, which is the expected signal from 1 GeV electron, the amplitude and time resolutions were $\sigma_A/A \approx 4\%$, and $\sigma_t \approx$100-150 ps (measured with a pulsed variable intensity UV laser). These tests served as a guide for specifying requirements for the procurement of the PMTs.

Following these tests, as a time and cost effective solution, Photonis XP3462B PMTs were chosen for the equipment of the HMS and SOS calorimeters. These 8-stage PMTs have a 3" diameter ($\approx$68 mm) semitransparent bi-alkaline photocathode, and a linear focused cube dynode structure with a peak quantum efficiency (QE) of $\sim$29% at 400 nm (Fig. 4). Using the criteria of high quantum efficiency, low dark current and high gain at relatively low HV, the best PMTs (150 out of 180 available) were selected. The negative operating voltages were set
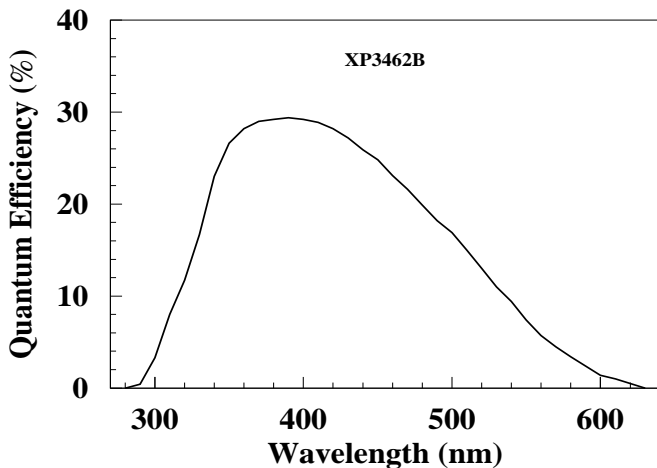
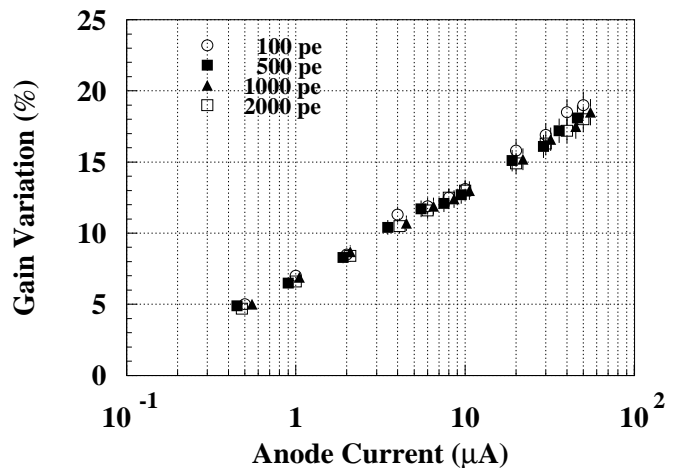FIG. 4: Typical quantum efficiency of the Photonis XP3462B PMT photocathode.

FIG. 5: An example of the gain variation of a XP3462B PMT with mean anode current measured at different light pulse heights, for the chosen HV distribution among the base dynodes (for details see Ref. [6]).

in the range ∼1.4-1.8 kV to match the gain ∼ 10^6. The outputs were gain matched to within ∼ 20%, and the remaining differences were corrected in software.

The PMT output signal may vary with respect to the incident photon's hit position on the photocathode. In general, this is caused by the photocathode and the multiplier (dynode section) non-uniformities. Although the focusing electrodes of a phototube are designed so that electrons emitted from the photocathode are collected effectively by the first dynode, some electrons may deviate from their desired trajectories causing lower collection efficiency. The collection efficiency varies with position on the photocathode from which the photoelectrons are emitted and influences the spatial uniformity of a PMT. The spatial uniformity is also determined by the photocathode surface uniformity itself. If the cathode-to-first dynode voltage is low, the number of photoelectrons that enter the effective area of the first dynode becomes low, resulting in a slight decrease in the collection efficiency.

For samples of PMTs the photocathode uniformity and effective diameter have been studied with a laser scanner. A ∼1 mm diameter fiber was positioned on the front of the PMT at a small distance from the photocathode. The light generated by the laser was split into two parts: one for the PMT scan, and another to monitor incident light intensity by a photo-diode. The PMT was mounted on a special stand, which could be moved remotely in 2-5 mm steps. At each position of the PMT, the coordinate information (x_i) from the scanner, PMT signal amplitude (A_{pmt}^i), and reference photo-diode signal (A_0) were read-out and written to a data file. The PMT photocathode uniformity and effective diameter were found from the analysis of the A_{pmt}^i/A_0 distribution versus x_i. Nearly all the tested XP3462B PMTs had a photocathode of good uniformity and effective diameter of no less than ∼2.8 inch. The measured effective diameter only weakly depends on the PMT high voltage. This is likely an indication that the effective diameter is largely determined by the collection efficiency between the photocathode and the first dynode.

Gain variation has been studied for the phototubes, under experimental conditions typical for CEBAF beam, as a function of the mean anode current, light pulse intensity and the high voltage distribution applied to the dynode system [6]. These studies suggest that at mean anode current ∼ 20 μA the PMT gain may change up to ∼ 15%. Examples of gain variation with mean anode current measured at the different light pulse heights are shown in Fig. 5.

Samples of the assembled modules were tested in a magnetic field to evaluate the quality of the PMT shields. At a fixed high voltage the blocks were illuminated through the ST connectors with a constant light intensity. Signal amplitude from the PMT was measured at gradually increasing values of the magnetic field. Measurements were performed at two different orientations of the PMT relative to the magnetic field: axial and transverse. As expected, the effect of the magnetic field was much stronger for the axial orientation. For both axial and transverse magnetic fields up to 2 Gauss, no effect was detected. Even at field values of about 4 Gauss, no effect was observed when the field was oriented transversely relative to PMT axis, while an axial field of the same strength reduced the PMT signal by 20–30%. We concluded that the PMT magnetic shields were sufficient, since in HMS and SOS detector huts the calorimeters are located far from the magnets where fringe fields are less that 0.5 Gauss.
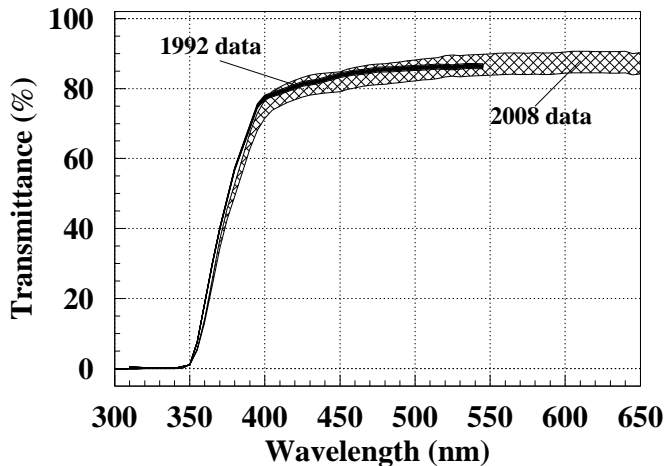
FIG. 6: The light transmittance efficiency of TF-1 type lead-glass blocks. The narrow dense band is data for unused blocks measured in 1992. New measurements on used SOS blocks, carried out in 2008, are shown in the hatched band.
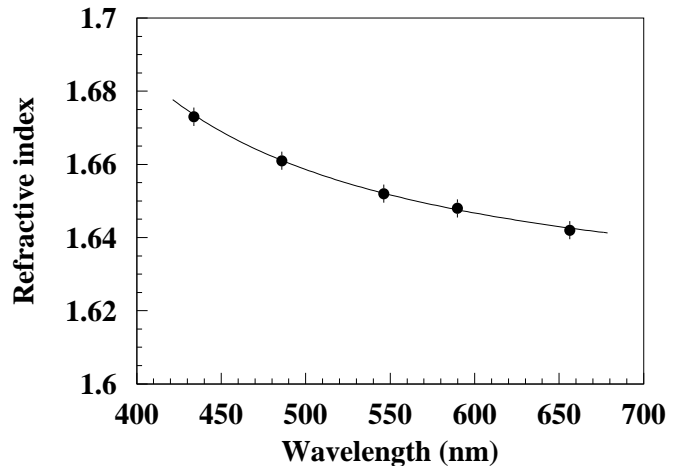

FIG. 7: Refractive index of TF-1 lead-glass versus wavelength. The filled circle symbols are measurements, the curve is a fit to them in the form $n_0 + \frac{n_1}{\lambda - \lambda_0}$, $n_0 = 1.617 \pm 0.004$, $n_1 = 10.4 \pm 2.3$, $\lambda_0 = 250.8 \pm 27.4$.

D. Studies on optical properties of TF-1 type lead glass blocks

With its index of refraction $\sim$1.65, radiation length 2.74 cm and density of 3.86 g/cm^3 TF-1 type lead glass is well suited for serving as Čerenkov radiator in electromagnetic calorimeters. Note, the TF-1 radiative length found in different sources varies from 2.5 to 2.8 cm. We cite the value obtained by means of PEGS4 (preprocessor for EGS4 [7]) and GEANT4 [8] packages. The fractional composition consists primarily of PbO (51.2%), SiO$_2$ (41.3%), K$_2$O (3.5%) and Na$_2$O (3.5%).

Before assembly, the light transmittance of all the blocks was measured using a spectrophotometer from the JLab Detector Group [9]. The wave-length was scanned from 200 nm to 700 nm in steps of 10 nm. The blocks were oriented transversely, and the light intensity passing through the 10 cm thickness was measured. Two measurements were carried out: with and without blocks (to subtract dark current of the light detector and light loss in air).

Those measurements were repeated in 2008 on a set of blocks taken from the decommissioned SOS calorimeter for re-use in the SHMS preshower counter. The blocks had been in use under the beam conditions for 15 years, and thus checks for possible degradation of the lead glass from radiation were necessary. Reliability of the measurements was checked by measuring spared, unused blocks and comparing with 1992 data.

Results from 1992 and 2008 measurements are compared in Fig. 6. Signs of marginal degradation can be noticed.

In 1992 the transmittance of some of the blocks had been measured in the longitudinal direction also. From pairs of the transverse and longitudinal measurements both refractive index (shown in Fig.7) and attenuation
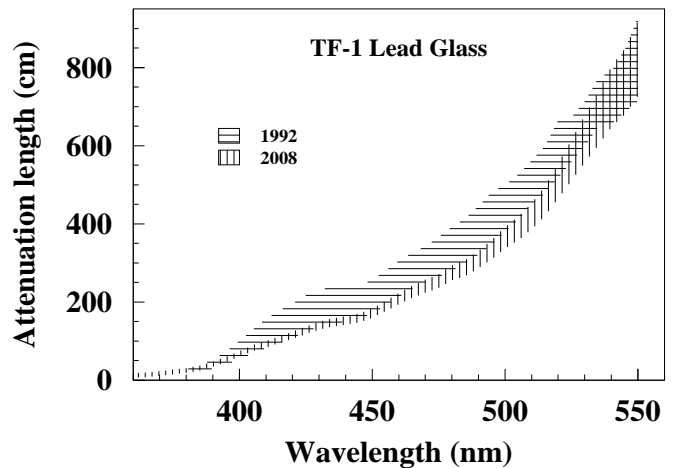

FIG. 8: Light attenuation length of TF-1 lead-glass obtained from transmission measurements of the glass blocks in early 1990's (horizontally hatched area) and in 2008 (vertically hatched area). The hatched area for the 1990's is bounded by the best and the worst cases, while the area for 2008 indicates the 2/3 majority of the cases.

length of the glass were extracted. From single measurements of the blocks in transverse orientation, only attenuation lengths are extracted by assuming the nominal refractive index of the glass of 1.65. As shown in Fig.8, the light attenuation length varies significantly in the range of sensitivity of the XP3462B photocathode, and is $\sim$100 cm at the peak of sensitivity $\sim$400 nm. The slight shift between 1992 and 2008 year measurements is partly due to different absolute calibrations of the setup.

The block to block variations in light transmission were compensated by pairing high quantum efficiency PMTs with low transparency blocks and vice versa in
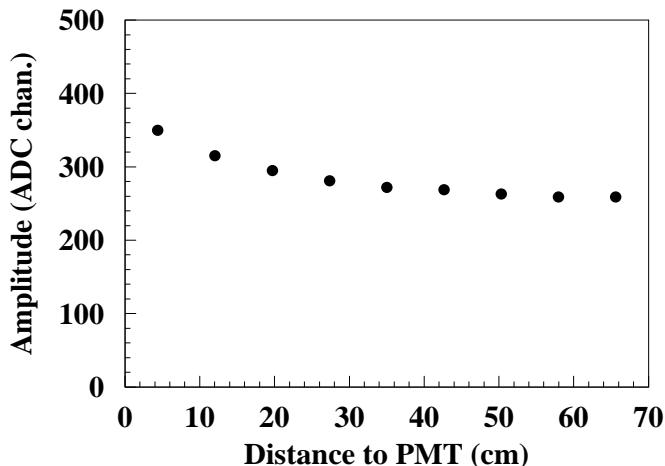
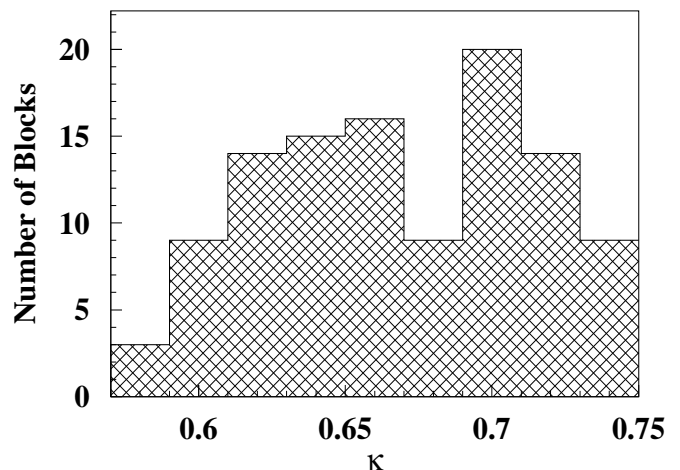FIG. 9: Response of a prototype module to cosmic rays passing at different distances to the PMT.

FIG. 10: The distribution of lead-glass blocks by $\kappa = A_{\text{Blue}}/A_{\text{Green}}$. See text for details. Blocks with $\kappa > 0.68$ were used in the SOS while the rest were used in the HMS calorimeter.

the module assemblies. Thus when all the PMTs were operated at a gain of $\sim 10^6$, the responses of modules to cosmic muons were equalized to within $\sim 20\%$. For straight through muons, signal of 60-70 photo-electrons on average from a block, and a pulse height resolution of $\sim 10 - 15\%$ were observed.

The response of a module to cosmic rays passing at different distances to the PMT was studied. Two small (5 cm $\times$ 5 cm) scintillator counters, placed on top and below the module and aligned vertically, were used to localize particles and to trigger signal readout. For single PMT modules, the signal variation at the edges was $\sim \pm 15 - 20\%$ relative to the center (shown in Fig. 9). For the two PMT modules, variation of the summed signal was on the level of $\sim \pm 7\%$ and the light output was about 1.5 times higher than for the single tube case [10].

The relative light transmittance of all the assembled modules was measured by use of green and blue Light Emitting Diodes (LEDs). The ratio of light transmission efficiency for blue and green LEDs, $\kappa = A_{\text{Blue}}/A_{\text{Green}}$, (see Fig. 10) depends on optical properties of the blocks and is a measure of block quality. As the SOS spectrometer typically detected lower momentum particles than the HMS, the blocks with higher κ, and thus a higher transmission efficiency for Čerenkov light, were used in the SOS calorimeter. This also had the benefit of ensuring to some extent uniformity in the calorimeters.

Final equalization of the PMT output signals, determination of the function parameters for amplitude–distance corrections and overall calibration of the calorimeters were performed with electron beam, by using "clean electron" data after their installation in the spectrometer detector huts.

E. Choice of high voltage divider

Special studies were performed to optimize the PMT high voltage base design for the requirements of good linearity (better than 1%), high rate capability and a weak variation of PMT gain with anode current [6]. Two manufacturers [11] recommended high voltage divider designs, optimized for high gain and linearity respectively. The bases had different relative fractions of the applied HV between the successive dynodes (from cathode to anode, including the focusing electrodes). We selected a design, which is a compromise between the two, but has also high anode current capability. This third design is a purely resistive, high current (2.3 mA at 1.5 kV), surface mounted divider (~ 0.640 $M\Omega$), operating at negative HV (see Fig. 11). The relative fractions of the applied HV between the dynodes (from cathode to anode) are: 3.12/1.50/1.25/1.25/1.50/1.75/2.00/2.75/2.75. The supply voltage for a gain of 10^6 is approximately 1750 V.

The PMT resistive base assembly is linear to within $\sim 2\%$ up to the peak anode current of 120 μA ($\sim 5 \times 10^4$ pe). The dark current is typically less than 3 nA. The base has anode and dynode output signals. Channel-to-channel adjustable high voltages are provided by a system of CAEN SY-403 high voltage power supplies (64 channel, $V_{max} = 3.0$ kV, $I_{max} = 3.0$ mA).

III. MONTE CARLO SIMULATION CODES

The first versions of simulation codes for the HMS/SOS calorimeters were based on the ELSS [12] and EGS4 [7] packages for simulations of electromagnetic showers. Dedicated code was added for Čerenkov light generation, optical photon tracing and photoelectron knockout from PMT photocathodes. The optics took into account light
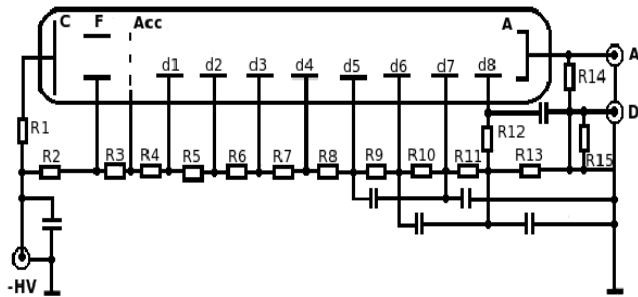
FIG. 11: Schematic of the high-voltage divider for XP3462B PMT. Selected with 1% tolerance and 1 W power resistors are: $R1 = 10\ M\Omega$, $R2 = 5.62\ k\Omega$, $R3 = 33.2\ k\Omega$, $R4 = 110.4\ k\Omega$, $R5 = 71.8\ k\Omega$, $R6 = R7 = R8 = R9 = 47.5\ k\Omega$, $R10 = 59.3\ k\Omega$, $R11 = 95\ k\Omega$, $R12 = 50\ \Omega$, $R13 = 71.8\ k\Omega$, $R14 = R15 = 1.0\ k\Omega$. All capacitors are 10 nF.

FIG. 12: Real (dashed line) and imaginary (solid line) refractive indexes of aluminum.

absorption in the lead glass, reflections from the block sides, and passage through the optical coupling to the PMT photocathode. However, the software did not take into account block to block variations of lead glass absorption length and electronic effects. The first simulations revealed sufficient signal ($\sim$900 photoelectrons from a 1 GeV incident electron), good linearity and reasonable resolution in the GeV range for the calorimeter designs.

Subsequent simulations of HMS calorimeter are based on the GEANT4 package, version 9.1. The QGSP_BERT physics list [13] was chosen to model hadron interactions, which is recommended by the GEANT4 developers for high energy physics calorimetry [14]. This list includes the parton string model [15] at energies above 12 GeV, intra-nuclear Bertini cascade [16] below 9.9 GeV, and a nuclear evaporation model [17] at low energies. The GHEISHA model [18] is used at energies 9.5 – 25 GeV. Electromagnetic processes are modeled to good accuracy within the framework of the GEANT4 standard electromagnetic package.

The code closely emulates the geometry and the composition of the detector. Particularly, the optical characteristics of the setup were thoroughly implemented in the light tracing part of the code summarized below. The light attenuation length is randomly varied from block to block within the observed experimental limits (see Fig. 8). The optical insulation of the module has multi-layer composition: air gap between aluminized Mylar and lead glass block, and Mylar support layer facing the block. The reflective and absorptive properties of aluminum reflector are expressed by means of real and imaginary parts of refractive index [19] (see Fig. 12).

Instead of GEANT4 optical photon handling, the generated light is traced by means of a dedicated fast Fortran code which takes care of the modular construction and is suited to the particular geometry of the module. Few compromises and simplifications took place in the code: a strict rectangular geometry of the glass blocks is as-
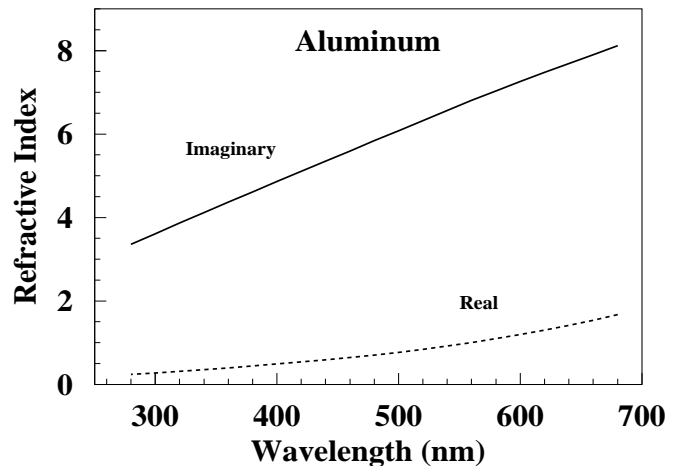
sumed; all the boundaries are flat and perfectly smooth, diffuse reflections from the walls are neglected; Rayleigh scattering in the glass is neglected as well; nor the polarization of Čerenkov light in the reflections/transmissions is taken into account.

Light reflectance from the block walls and passage from block to PMT photocathode is treated as reflection/transmission from/through a plane-parallel plate sandwiched between two optical media of different refractive indices. In the first case it is a layer of air in between the lead glass and the reflector aluminum, in the second case it is a layer of optical grease between the lead glass and PMT window glass. The layers are assumed thin enough to neglect light absorption, and thick enough to neglect light interference effects. With these assumptions, expressions for reflectivity and transmittivity of the boundaries were derived in the limit of infinite series of Fresnel reflections/transitions from the surfaces of the plate (similar to [20], p. 360).

This model was checked against GEANT4 calculations, and good agreement was found between the two. In terms of the detector signal, the difference was less than a few percent.

A typical quantum efficiency of XP3462B photocathode (Fig. 4) is assigned to all the PMTs. Electronic effects are taken into account by assigning a random multiplicative "gain" factor to each channel in order to transform the number of photoelectrons into ADC channels. This factor is varied from channel to channel by 50% around a mean value of 2. The electronic noise is modeled by adding a random pedestal of normal distribution with $\sigma = 10$ ADC channels. Both, the "gain" factor and the pedestal width roughly correspond to experimental conditions.

The projectiles are sampled at the focal plane of the spectrometer using the coordinate, angular and momentum distributions observed in the Meson Duality experiment [21]. The momenta are scaled to the settings of the

TABLE II: Materials between HMS focal plane and calorimeter that are taken into account in the simulation. The listed positions are at the fronts of components

Component	Material	position (cm)	thickness (cm)	density (g/cm^3)
DC2 gas	Ethane/Ar	29.3	15	0.00143
DC2 foils	Mylar		2×0.00254	1.4
S1X hodoscope	BC408 scint.	77.8	1.067	1.032
S1Y hodoscope	BC408 scint.	97.5	1.067	1.032
Aero. entrance	Al	40	0.15	2.6989
Aero. radiator	Aerogel		9	0.152
Aerogel air gap	air		25.5	0.0012
Aerogel exit	Al		0.1	2.6989
Gas Č gas	C_4F_1O	198	150	0.0047
Gas Č wind.	Al		2×0.1	2.6989
Gas Č mir.sup.	Rohacell	230	1.8	0.050
S2X hodoscope	BC408 scint.	298.8	1.067	1.032
S2Y hodoscope	BC408 scint.	318.5	1.067	1.032
Calo. support	Al	350	0.55	2.6989

studies.

Material traversed by particles before reaching the calorimeter smears the energy and coordinates of the particles. Therefore, all the material between the focal plane and calorimeter is also modeled (see Table II).

IV. ELECTRONICS AND CALIBRATION

A. Electronics

The readout electronics were identical for both calorimeters. The raw anode signals from the phototubes were taken from the detector hut to the electronics room through ∼30 feet RG58, then ∼450 feet RG8 coaxial cables. The signals were then split 50/50, with one output sent through 400 ns RG58 delay cable to a 64-channel LeCroy 1881M Fastbus ADC module, and the other to a Philips 740 linear fan-in modules to be summed. A schematic diagram of the electronics for the calorimeters is shown in Fig. 13.

Data from the Fastbus modules were acquired in the "sparsified" mode, in which only significant data were read from each ADC channel. The ADCs have programmable thresholds which were set ab initio fifteen channels above zero. The zero (or "pedestal") of an ADC channel was determined at the beginning of each run by creating 1000 artificial triggers. These thousand events show up as a narrow peak in a histogram of an ADC output. Typical pedestal widths were about 5-7 channels for the ADC gate width ∼100 ns. Then the new threshold for each ADC channel was calculated as three times the width above the pedestal. The automatically determined thresholds then can be used as input to the data acquisition code such that it only reads out above the threshold, hence minimizing data flow.
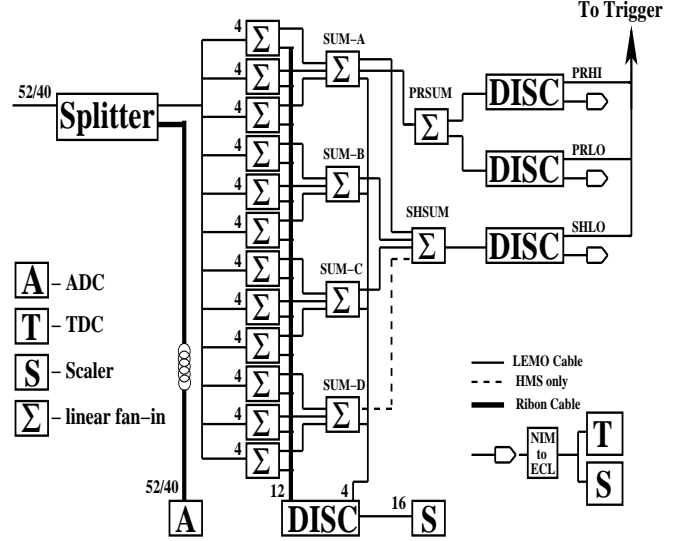

FIG. 13: Calorimeter electronics diagram. The numbers indicate the number of channels used in the HMS/SOS. For the SOS, the 4-th layer sum was not included in the trigger. Adapted from [22].

Because of the high pion to electron ratio for some of the experiments, events are required to pass loose particle identification cuts before generating a trigger. In order to have a high efficiency for electrons, a trigger was accepted as an electron if either the gas Čerenkov detector fired or if the electromagnetic calorimeter had a large enough signal. The threshold on the gas Čerenkov counter signal was typically set near the 1 pe level, and the threshold on the calorimeter signal was set just above the pion peak, which is independent of the spectrometer momentum setting. This allowed for extremely high electron efficiency even if one of the two detectors had a low efficiency. On the other hand, the pion rejection was conditioned by the low, in this case, threshold on the calorimeter signal.

Raw signals from the whole calorimeter and from the front layer alone are summed for use as an option in the first level electronic trigger for e/π discrimination [22]. The fourth layer of the SOS calorimeter is not summed, since due to the 1.74 GeV maximum electron energy in the SOS, most of the electromagnetic shower is contained in the first 3 layers, and removing the last layer has almost no impact on the electron signal, but reduces the pion signal (for straight through pions by 25%). The sum in the first layer (PRSUM) and the sum in the entire calorimeter (SHSUM) are discriminated to give three logic signals for the trigger: PRHI and PRLO are high and low threshold signals from the first layer, and SHLO from the entire calorimeter. Also, groups of four modules are summed and sent through discriminators to scalers in order to call attention to dead or noisy tubes.

The electron trigger (ELREAL) had two components: Electron High (ELHI) and Electron Low (ELLO). ELLO was designed to trigger for all electrons, even those de-

positing low shower energy. Thus, it provided increased efficiency at the low electron momenta. ELLO required a Čerenkov detector signal, a hodoscope signal (SCIN), and a shower signal (PRLO). ELHI required a high calorimeter signal, but no Čerenkov detector signal, and it was composed of preradiator high signal (PRHI), a three-out-of-four coincidence scintillator signal (SCIN) and the shower counter signal (SHLO).

B. Calorimeter Calibration

The ability of particle identification of a calorimeter is based on differences in the energy deposition from different types of projectiles. The deposited energy is obtained by converting the recorded ADC channel value of each module into equivalent energy. To obtain an accurate measurement of it, two main issues must be overcome: the light attenuation in the lead-glass block, and block to block PMT gain variation.

To correct the attenuation, the signal from each block is multiplied by a correction factor that depends on track position. This correction factor was different for the blocks with one and two PMT readouts. The correction was checked by looking at the distributions of corrected energy as a function of distance from the PMTs.

The PMT gains had been matched in the hardware in order to make the calorimeter trigger uniform within acceptances of the calorimeters as much as possible. At first, using scattered electrons in each spectrometer the operating high voltages for the PMTs were adjusted so that the ADC signals were nearly identical (to $\sim 10\%$) for blocks in the same layer. Electrons with larger momenta are bent less in the spectrometer, and populate the bottom blocks in the calorimeter. Because the bottom blocks detect higher energy electrons, their gain must be kept lower than for the top blocks so that the output signals are of the same size. Therefore, setting the gain such that the output signal is constant as a function of vertical position in the calorimeter means having a gain variation between the blocks roughly equal to the momentum acceptance of the spectrometers ($\sim 20\%$ in the HMS, $\sim 40\%$ in the SOS). The output signals were made equal (rather than gains) in order to make the calorimeter trigger efficiency as uniform as possible over the entire calorimeter.

The data analysis procedure corrects for the gain differences in the process of calorimeter calibration. Good electron events are selected by means of gas Čerenkov detector. The standard calibration algorithm [23] is based on minimization of the variance of the estimated energy with respect to the calibration constants, subject to the constraint that the estimate is unbiased (relative to the primary energy). The momentum of the primary electron is obtained from the tracking in the magnetic field of the spectrometer.

The deposited energy per channel is estimated by

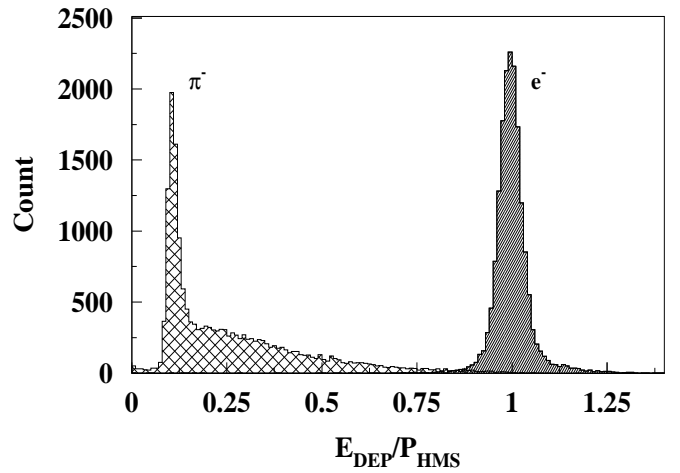$$e_i = c_i \times (A_i - ped_i) \times f(y), \tag{1}$$

FIG. 14: Energy deposition in the HMS calorimeter from 3 GeV/c pions (hatched histogram) and electrons (filled histogram) in E01-004 (Fpi-2) experiment.

where i is the channel number, c_i is the calibration constant, A_i is the raw ADC signal, ped_i is the pedestal position, $f(y)$ is correction for the light attenuation for the horizontal hit coordinate y.

Due to the segmentation in the vertical direction, the calorimeters have a coarse tracking capability which is helpful when separating multiple tracks (see, for instance, [24]), [25]). In the calorimeter analysis code hits on adjacent blocks are grouped into clusters for which the deposited energy and center of gravity are calculated. These clusters are matched with tracks from the upstream detectors if the distance from the track to cluster in the vertical direction is less than a predefined "slop" parameter (usually 7.5 cm).

The calorimeter energy corresponding to a track is divided by the track momentum and used for particle identification. In the few GeV/c range pions and electrons are well separated (see Fig. 14), a cut at 0.7 ensures an electron detection efficiency better than 99% and 30:1 pion suppression (see [26] and Section V).

V. PERFORMANCE OF HMS/SOS CALORIMETERS

A. Selection of calorimeter experimental data

For these studies, HMS calorimeter data from the E01-004 (Fpi-2) [27] and E00-108 (Meson Duality) [21] experiments have been collected for comparison with simulations. Fpi-2 measured the charged pion form factor at Q^2=1.6 and 2.45 (GeV/c)^2 via exclusive pion production, while Meson Duality looked for signatures of quark-hadron duality in semi-inclusive pion production. The experiments ran back to back in summer of 2003, and both detected pions in the HMS in coincidence with

electrons in the SOS. Fpi-2 also detected electrons at elastic kinematics for HMS acceptance studies. Some other JLab experiments also used HMS or SOS calorimeters for good pion rejection and studied the devices, such as E89-008 [22], E02-019 [30], E03-103 ([29], [31]).

In order to obtain high purity samples of electrons and pions, tight cuts were applied to spectrometer events. Only events with single tracks in HMS and SOS passing through the collimators were used. Spectrometer acceptances were restricted to ensure good tracking accuracies, and, on the HMS side, efficient particle identification with gas Čerenkov counter. Electrons in HMS were identified by applying a high cut on the gas Čerenkov signal greater than 4 photoelectrons, while pions were identified with null signal.

Pion samples were selected in the HMS from $(e'\pi)$ coincidence events, by posing tight electron PID cuts on the SOS gas Čerenkov detector signal greater than 3 photoelectrons, and normalized energy deposition in the SOS calorimeter E_{Dep}/P_{SOS} greater than 0.9. Furthermore, a coincidence timing cut |cointime|<1 ns was also applied. Accidental events were selected and subtracted from energy deposition histograms by off coincidence timing cut $3 <$|cointime|< 13 ns.

In addition, a kinematic cut of exclusive pion production on the missing mass was applied for Fpi-2. Finally, for these studies HMS calorimeter was calibrated on a run by run basis. Examples of the resultant distributions of the energy depositions in the calorimeter from incident electrons and pions are shown in Fig. 14.

B.   Resolution of HMS/SOS calorimeters

We define calorimeter resolution as the width of a Gaussian fit to the electron peak (Fig. 14) in the distribution of energy deposition.

The resolution of HMS calorimeter from a number of Hall C experiments is compared with simulation in Fig. 15. Experiments before the modification of the detector in 1998 (see subsection II B), like E89-008 shown in the figure, report resolution $\sim 6\%/\sqrt{E}$ (E in GeV) ([22], [28]). Experiments carried out afterward found improved energy resolution. Exception is the E99-118 experiment [25] with resolution $8\%/\sqrt{E}$. E00-116, the first experiment to actually analyze data with the modified calorimeter, states resolution $5.4\%/\sqrt{E}$ [26]. E03-103, despite of a gain shift problem in the calorimeter electronics, obtained somewhat scattered data close to the simulation [29]. E04-001 got very good resolution in the wide range of HMS momenta, in agreement with simulation, presumably due to relatively low rate, good tracking conditions, and run by run calibration [33]. A somewhat worse resolution is obtained from online analysis of the E01-006 [32] experiment at high energies up to ∼4.7 GeV/c.

As for the SOS calorimeter, an on-line data analysis during the Hall C Spring03 experiments (E00-002, E01-
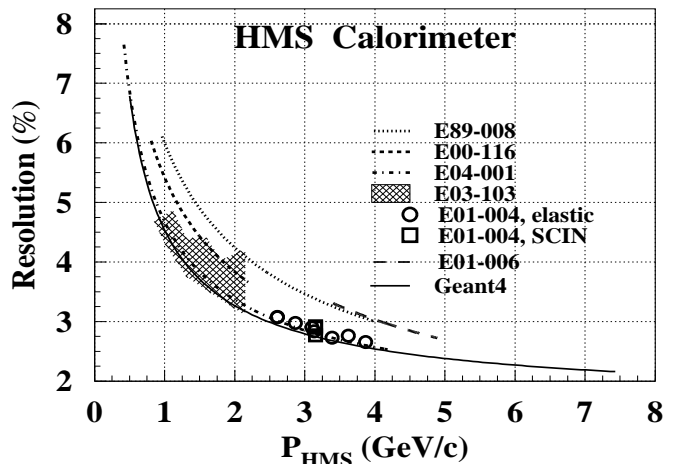

FIG. 15: Resolution of the HMS calorimeter. Dotted, dashed, dash-dotted and long-dashed lines are fits to data taken from E89-008 [22, 28], E00-116 [26], E04-001 [27] experiments, and from online analysis of E01-006 [32] experiment respectively. The dashed area represents scattered data from E03-103 [29] experiment. The empty symbols are our re-analysis of the E04-001 experiment. The solid line is a fit to the GEANT4 calculations (see text for details).

002, E00-116) gave a resolution of $6\%/\sqrt{E} + 1\%$, within the range of SOS momentum setting 0.5 – 1.74 GeV/c. The E00-108 experiment reported a resolution consistent with $\sim 5\%/\sqrt{E}$ for SOS momentum range 1.2 – 1.7 GeV/c [34].

In general, resolution from an experiment depends on multiple factors related both to hardware and software. Some of them, like trigger rate, background rate, performance of tracking detectors, tracking algorithm itself affect performance of the calorimeter indirectly, through the tracking conditions. Other factors, like electronic noise, stability of high voltage supply, low energy background, calibration affect the performance directly.

The conventional 3-parameter fit [36] to the simulated HMS resolution (in %) gives a dependence on energy in the form $3.75/\sqrt{(E)} \oplus 1.64 \oplus 1.96/E$. The first term is purely of stochastic origin, the second term reflects systematics from non-uniformity of the detector and calibration uncertainty, the third term, poorly constrained here by limited statistics, comes from electronic noise. In the simulated data stochastic and systematic terms dominate, electronic noise is tangible only at low energies $\lesssim$1.5 GeV.

Overall, the resolution of the HMS/SOS calorimeters is close to resolutions of the lead-glass calorimeters of similar thicknesses (see [37] and references therein, also [38, 39]).
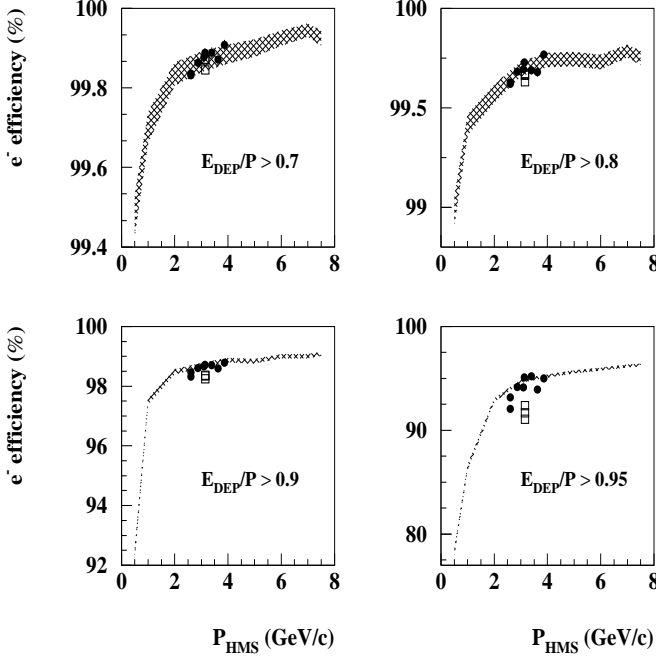
FIG. 16: Efficiency of electron detection in HMS calorimeter at different momenta and for different cuts on the normalized energy deposition. The shaded areas represent results from GEANT4 simulations. The solid circles and empty boxes are data from Fpi-2 experiment taken at elastic scattering kinematics and from exclusive pion production respectively.

C. Electron detection efficiency and pion rejection

The experimental efficiency of electron detection, which is defined as the fraction of events with the normalized energy deposition above threshold, at momenta within the range 2.8–4.1 GeV/c, for different cuts is in reasonable agreement with the simulation (see Fig. 16). The simulation predicts a steady rise of e^- detection efficiency with energy due to the improvement in resolution. However, as shown in Fig. 17 there is a growing disagreement with experiment for energies below 2 GeV.

The π^- suppression factor, the ratio of total number of pionic events and misidentified as pions, at different momenta and cut values is shown in Fig. 18. Experimental data for comparison are mostly from the Meson Duality experiment. At 3 GeV/c there are data from Fpi-2 as well. The Fpi-2 data are presumably of better quality due to favorable background conditions and exclusive kinematics for pion production. Good agreement between the two experiments at 3 GeV ensure the quality of the pion suppression data found in Meson Duality.

Both experiment and simulation show a momentum dependence of the suppression factor peaking at several GeV/c. While in the experiment the peak value is reached at ~ 2.5 GeV/c independent of the cut, in the Monte Carlo it shifts to higher momenta as the cut is raised. Overall, agreement between experiment and sim-
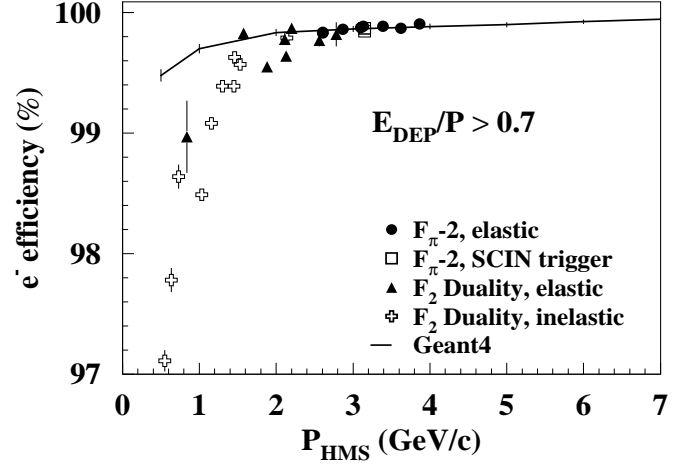

FIG. 17: Efficiency of electron detection in HMS calorimeter versus momentum of the spectrometer, with cut on the normalized energy deposition at 0.7. GEANT4 simulation is compared to the Fpi-2 reanalysis and data from the inclusive resonance electroproduction experiment [28].

ulation is satisfactory for the rejection studies.

Few Hall C experiments report on the rejection capabilities of HMS or SOS calorimeters. E89-008, the first Hall C experiment [22] states pion suppression by 25:1 for $E_{Dep}/P > 0.7$ at 1 GeV/c HMS momentum, which agrees with experimental data in this study, and fast improvement with energy due to moving the threshold to higher positions. E94-014 reports a pion rejection 95% at SOS momenta 1.4-1.5 GeV/c for the cut value of 0.7 [40]. Note that these two experiments ran before the calorimeters had been modified. The same rejection is reported in E00-108 for HMS at 1.7 GeV/c [34], again in rough agreement with this study. The higher suppression factor obtained in this study comes from the cleaner selection of the particle samples (see subsection V A).

Segmentation of HMS calorimeter allows for using the difference in longitudinal development of electromagnetic and hadronic showers for PID. In particular, energy deposition in the forward layer is most indicative. This is elaborated in subsection VI F, with regard to the SHMS calorimeter. As it is seen in Fig. 19, one can gain substantially in PID capability of the HMS counter, by combining energy depositions in the first layer and in the whole calorimeter. Relative to the ordinary rejection, at the 3 GeV/c spectrometer setting, improvement in pion suppression is more than twice at low electron detection efficiencies 90 – 95%, and ~ 1.5 times at high efficiencies above 99.7%. Alternatively, one can keep the suppression factor constant and gain in detection efficiency. For instance, at 250:1 π^- suppression factor one can boost e^- detection efficiency from $\sim 93\%$ to $\sim 98.5\%$.
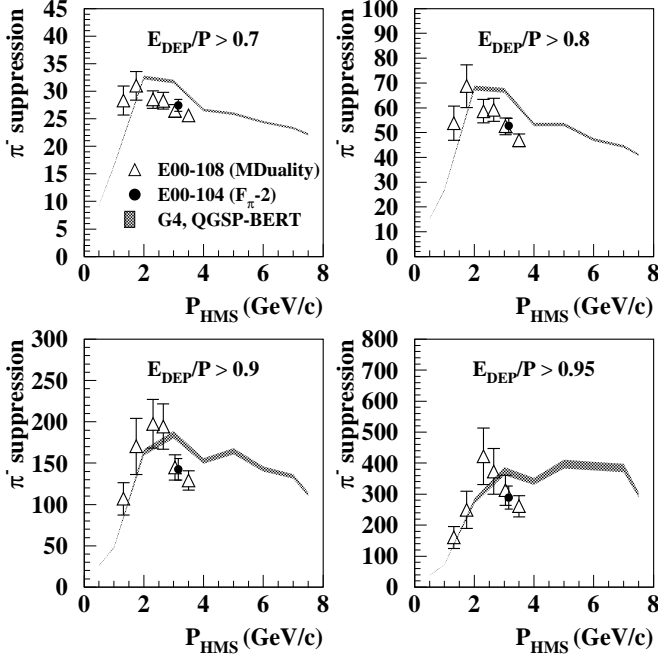
FIG. 18: Pion suppression factor of HMS calorimeter versus momentum of the spectrometer at different cuts on the normalized energy deposition. The GEANT4 simulation (shaded area) is compared to data from Meson Duality and Fpi-2 experiments. A cut on the missing mass is added for the selection of exclusive pion production in Fpi-2.
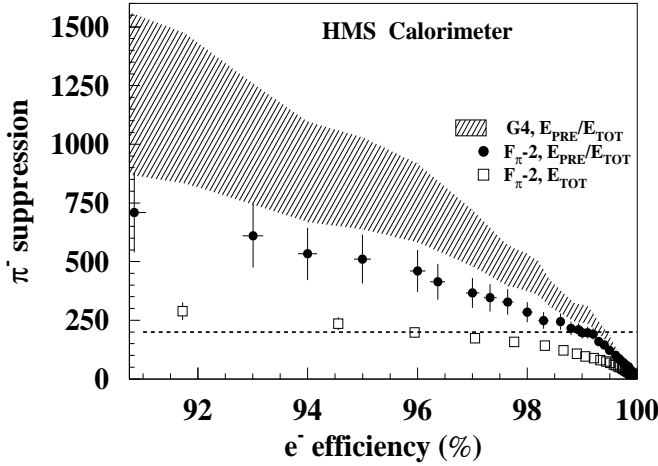

FIG. 19: π^- suppression factor versus e^- detection efficiency from 2-dimensional Preshower/Shower separation (closed symbols) and ordinary 1-dimensional rejection (open symbols) in HMS calorimeter, obtained from analysis of Fpi-2 [35] experimental data at 3.153 GeV/c HMS setting. Here, the forward layer of the detector served as the Preshower. The shaded area represent results from GEANT4 simulation on the 2-dimensional separation at 3 GeV/c.

D. Long-term stability of calorimeters

The HMS/SOS calorimeters' resolution shows only slight changes during the years of usage (see Fig.15). These changes include variations in electronics, calibration technique and possible degradation of the calorimeter components.

Stability of both calorimeters also has been evaluated by tracking changes in the ADC pedestal and PMT gain values. These values have been found to be stable within accuracy of the measurements during the entire time of operation. The long-term stability of the calorimeters' responses have been monitored by tracking the variations in the width of normalized energy deposition (E/p) distribution, and variations in the PMT gain calibration constants from run to run, and from experiment to experiment. No significant degradation of HMS/SOS calorimeters' performances after 15 years of operation have been noticed.

VI. SHMS CALORIMETER

A. Design construction

As a full absorption detector, the SHMS calorimeter is situated at the very end of detector stack of the spectrometer [2]. The relatively large beam envelope of the SHMS dictated a different calorimeter design from HMS/SOS, with a wider acceptance coverage. In order to exclude possible energy leaks at higher energies, it was necessary to consider a shower counter for SHMS thicker than in HMS. The deeper calorimeter, the less energy leak of the electromagnetic shower from the radiator, but more light loss due to absorption in the glass and reflections is expected. Therefore, there should be an optimum in the detector dimension along the particle trajectory. For an energy range of a few tens of GeV it was found that the optimum is at the radiator length of ∼40 cm [41, 42].

The general requirements for the SHMS calorimeter are:
- Effective area: 120×140 cm^2;
- Total thickness: ∼20 rad. length;
- Dynamic range: 1.0 - 11.0 GeV/c;
- Energy resolution: $\sim 6\%/\sqrt{E}$, E in GeV;
- Pion rejection: ∼100:1 at $P \gtrsim 1.5$-2.0 GeV/c;
- Electron detection efficiency: > 98%.

B. Studies of different versions and choice of assembling

A few different versions of calorimeter assembly for the SHMS spectrometer have been considered ([43–45]) before it was optimized for cost/performance. A possible choice is a construction similar to the HMS and SOS calorimeters. An alternative is a calorimeter similar to

HERMES [37] and Hall A [46] shower counters. The goal of these studies was to explore a few proposed versions of the SHMS calorimeter based on commercially produced lead glass.

The configurations considered are a total absorption part (called Shower in the following), or a combination preshower and shower parts ("Preshower+Shower" in the following). The Preshower is a slab of a few radiative length thick lead-glass before the Shower part. For each version the energy resolution, electron detection efficiency and pion/electron separation capabilities were determined by simulations. The Shower and Preshower were made from modules, which consist of an optically isolated rectangular lead-glass block and optically coupled to it a PMT.

For all versions we assumed only modular construction of the calorimeters since this gives more flexibility in assembling and allows for localizing the position of energy deposition clusters. Different types and sizes of the lead-glass blocks were also considered. We found the energy resolution for all versions with and without Preshower to be nearly similar, but different versions required different number of modules (channels) to cover the acceptance of the SHMS. Adding a Preshower dramatically improves the π/e rejection factor.

Our studies allowed selection of the optimum calorimeter geometry while maintaining the good energy resolution and pion rejection capabilities. The newly designed SHMS calorimeter consists of two parts (see Fig. 20): the main part at the rear (Shower), and Preshower before the Shower to augment PID capability of the detector. An optimal and cost-effective choice was found by using available modules from HERMES calorimeter for Shower part, and modules from SOS calorimeter for Preshower. With this choice the Shower becomes 18.2 radiative length deep and almost entirely absorbs showers from ∼10 GeV electromagnetic projectiles, and Preshower becomes 3.6 radiation length thick.

C. Description of constructive elements

The SHMS Preshower radiator consists of a layer of 28 TF-1 type lead glass blocks from the calorimeter of the retired SOS spectrometer in Hall C, stacked in two columns in an aluminum enclosure (not shown in Fig. 20). 28 PMT assemblies, one per block, are attached to the left and right sides of the enclosure. The Shower part consists of 224 modules from the decommissioned HERMES detector [37] stacked in a "fly eye" configuration of 14 columns and 16 rows. ∼ $120 \times 130\,\mathrm{cm}^2$ of effective area of detector covers the beam envelope at the calorimeter.

The Preshower enclosure adds little to the material on the pass of particles. On the front and back are 2" Honeycomb plate and a 1 mm sheet of aluminum respectively, which add up to 1.7% of radiation length only. The optical insulation of the 10 cm × 10 cm × 70 cm TF-1 blocks (see Section II for details) in the Preshower is optimized
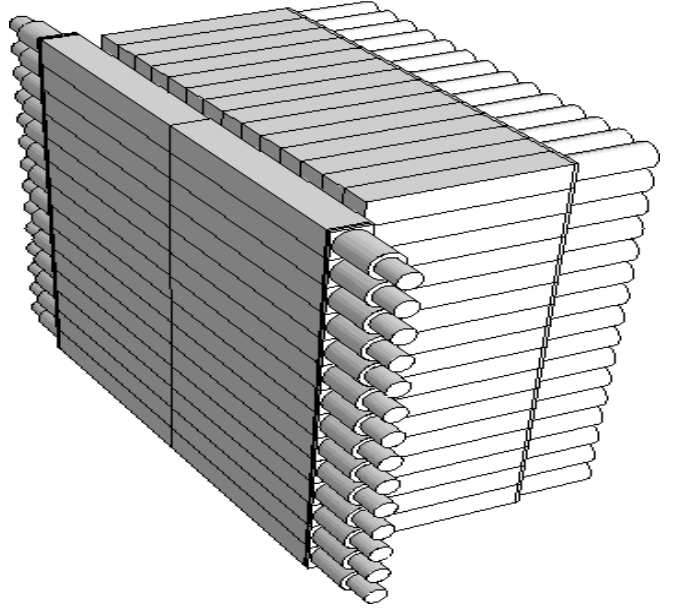

FIG. 20: A sketch of SHMS calorimeter. Shown are Preshower (on the left) and Shower parts. Support structures are omitted.

to minimize the dead material between them, without compromising the light tightness. First, the blocks are loosely wrapped in a single layer of 50 μm thick reflective aluminized Mylar film, with Mylar layer facing the block surface. Then, every other block is wrapped with a 10 cm wide strip of 50 μm thick black Tedlar film, to cover its top, bottom, left and right sides but the circular openings for the PMT attachments. Looking at the face of detector, the wrapped and unwrapped blocks are arranged in a chess pattern. Insulation of the remaining front and back sides of the blocks are provided by facing inner surfaces of the front and rear plates of the enclosure, covered also with Tedlar. In addition, a layer of Tedlar separates the left and the right columns.

The PMT assembly tubings are screwed in 90 mm circular openings on both sides of the enclosure. The spacing of the openings matches the height of the blocks, so that a PMT faces to each of the blocks. The 3" XP3462B PMTs are optically coupled to the blocks using ND-703 type Bycron grease of refractive index 1.46.

The HERMES modules to be used in the Shower part are similar in construction to the HMS/SOS modules but differ in details. The radiator is an optically isolated $8.9 \times 8.9 \times 50\,\mathrm{cm}^3$ block of F-101 lead-glass, which is similar to TF-1 in physical parameters. The typical density of F-101 type lead-glass is 3.86 g/cm^3, radiation length 2.78 cm, and refraction index 1.65. The chemical composition of F-101 is: Pb_2O_4 (51.23%), SiO_2 (41.53%), K_2O (7%) and CeO (0.2%) by weight [41]. The small amount of Cerium, added for the sake of radiation hard-
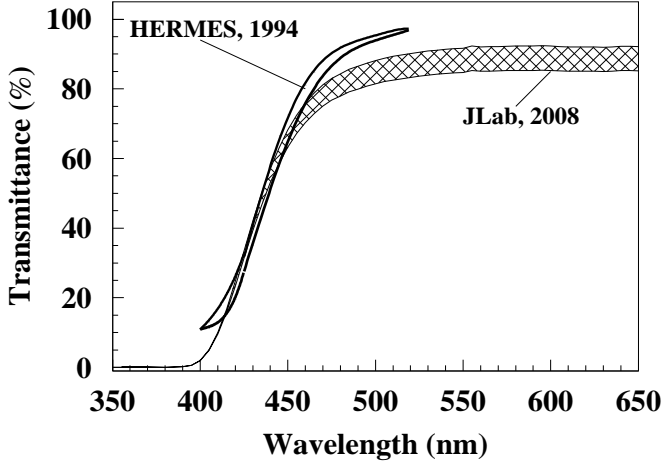
FIG. 21: Transmittance of unused (not radiated) F-101 lead-glass blocks. The hatched area represents results from JLab 2008 year measurements, narrow band within solid lines is 1994 year data from HERMES collaboration [41].
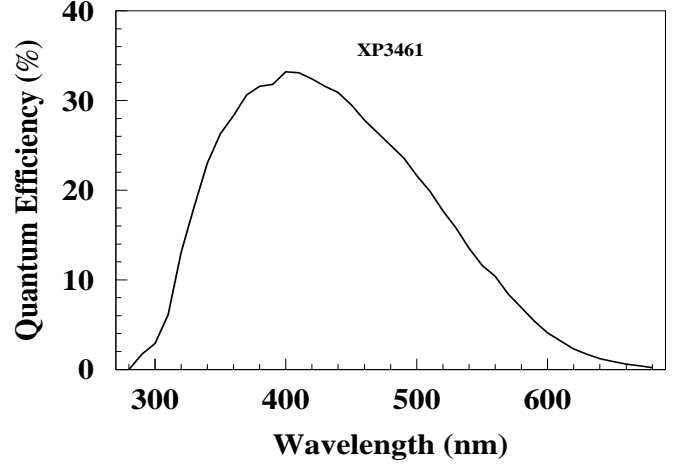

FIG. 22: Typical quantum efficiency of a photocathode of the XP3461 PMT used in the simulation, derived from the typical radiant sensitivity from the vendor.

ness ([47], [48]), absorbs light at small wavelengths, and thus restricts the band of optical transparency to higher wavelengths (see Fig. 27).

Results of F-101 type lead-glass block transmittance measurements are shown in Fig. 21. For unused blocks, a $\sim 10\%$ shift in transmittance has been found between the 1994 year measurements by the HERMES collaboration [41] and our measurements at JLab in 2008. We believe that the shift between the two sets of measurements is due to different calibration techniques of the setups.

Each F-101 block is coupled to a 3" XP3461 PMT from Photonis, with green extended bialkali photocathode, of the same sizes and internal structure as the XP3462B in the HMS/SOS calorimeters and in the Preshower. Typical quantum efficiency of the photocathode is $\sim 30\%$ for $\lambda \sim 400\ nm$ light (see Fig. 22), and the gain is $\sim 10^6$ at ~ 1500 V. Silgard-184 silicone glue of refractive index 1.41 is used for optical coupling of the PMTs to lead-glass blocks.

A μ-metal sheet of 1.5 mm thickness and two layers of Teflon foil are used for magnetic shielding and electrical insulation of the PMTs. The blocks are wrapped with 50 μm aluminized Mylar and 125 μm black Tedlar paper for optical insulation. A surrounding aluminum tube which houses the μ-metal, is fixed to a flange, which is glued to the surface of the lead-glass. The flange is made of titanium, which matches the thermal expansion coefficient of F-101 lead-glass [41].

Beyond simple repairs, no adjustment has been made to the original HERMES construction of the modules for re-use in the SHMS calorimeter.

D. Pre-assembling checks and tests

As both the TF-1 and F-101 lead-glass blocks have been in use for more than 14 years under conditions of high luminosity, there was concern about possible radiation degradation of the blocks and the PMTs. Changes in transparency of TF-1 and F-101 lead-glasses, irradiated with 70 GeV protons and 30 GeV π^- mesons have been reported in [49]. It was found that the resistance of TF-1 lead-glass against irradiation is 50 times less than that of F-101. An accumulated dose of 2 krad produces a degradation of transmittance of F-101 glass of less than 1%. It was also found that the darkening of lead-glass radiators due to irradiation can be considerably reversed by intensive light illumination. Ref. [50] reports that exposure of radiation-damaged glass to UV irradiation or to high temperature can bring about recovery of the glass.

The changes in transparency of TF-1 and F-101 type lead-glass radiators have been studied in [45, 51]. The estimated radiation dose for the used blocks was about 2 krad. For several samples of F-101 and TF-1 type blocks the light transmittance has been measured before and after 5 days of curing with UV light (of wavelength λ=200-400 nm). The transmission for F-101 type blocks from HERMES before and after the UV curing is shown in Fig. 23. We do not find significant changes in transmittance.

Note that for the TF-1 type blocks taken from the SOS calorimeter, our measurements again show negligible degradation over more than 15 years of operation (see Fig. 6 in Section II D). This is due to efficient shielding of the SOS (HMS) spectrometer detector huts.

To summarize the results of our studies on the radiation effects, there is no evidence for noticeable radiation damage of TF-1 and F-101 lead-glass blocks to be used in the construction of the calorimeter for SHMS spectrom-
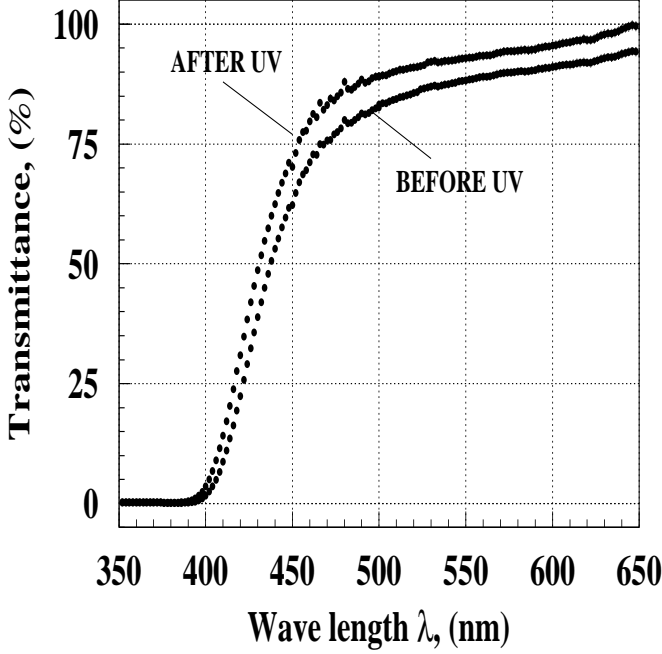
FIG. 23: Radiated (∼2 krad) F-101 type lead-glass blocks transmission efficiencies before and after 5 days of UV curing.
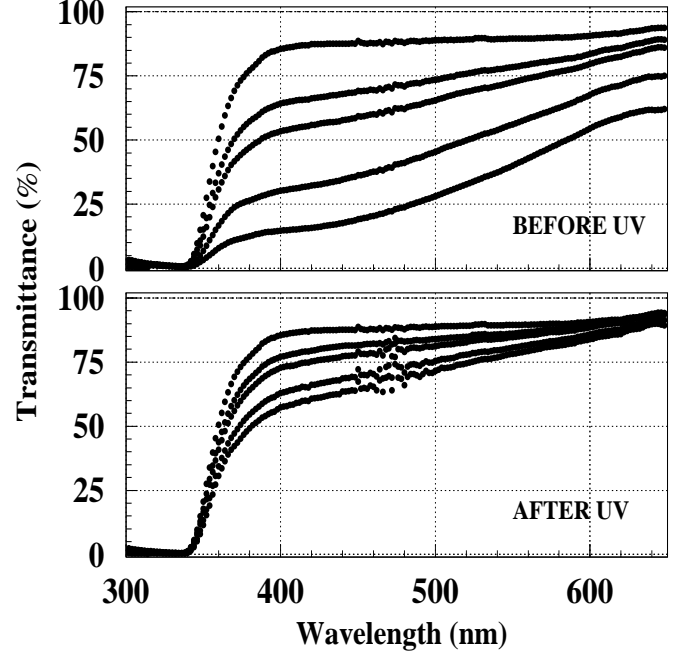

FIG. 24: Radiated (∼2-6 krad) TF-1 type lead-glass blocks' transmittance before (top panel) and after 5 days of UV curing (bottom panel).

eter.

As a cross check, we performed similar studies for the TF-1 type lead-glass blocks taken from the BigCal calorimeter, which had been used in Hall C experiment Gep-III [52]. This calorimeter was operated in open geometry, and accumulated a dose of ∼2-6 krad. The results presented in Fig. 24 show the effect of UV curing, indicating strong radiation degradation.

The gain and relative quantum efficiencies for randomly selected PMTs from the SOS calorimeter (XP3462B) and from the HERMES detector (XP3461) have been measured to check possible degradation effects in the PMTs. A simple setup with a LED light source was used to localize the Single Electron Peak (SEP) at a given HV and define the gain for each PMT.

Examples of gain variation versus high voltage for the Photonis XP3462B PMT are shown in Fig. 25. While 1992 and 2010 data sets agree within the errors, a systematic offset of ∼ 10 − 15% can be seen between the two, which is related to different setups used in the measurements.

For a set of PMTs dismounted from HERMES modules we have compared relative quantum efficiencies with new XP3461 PMTs. The HV for each PMT was adjusted to the gain ≈ 1.5 × 10^6. The light intensity was adjusted to get about 100 photoelectrons from the unused new PMTs, and this intensity was monitored by a reference PMT. Since we kept the LED at fixed intensity and operated all the PMTs at a fixed gain, the difference between the detected number of photoelectrons may only come from the difference in the PMT QEs. The number of de-
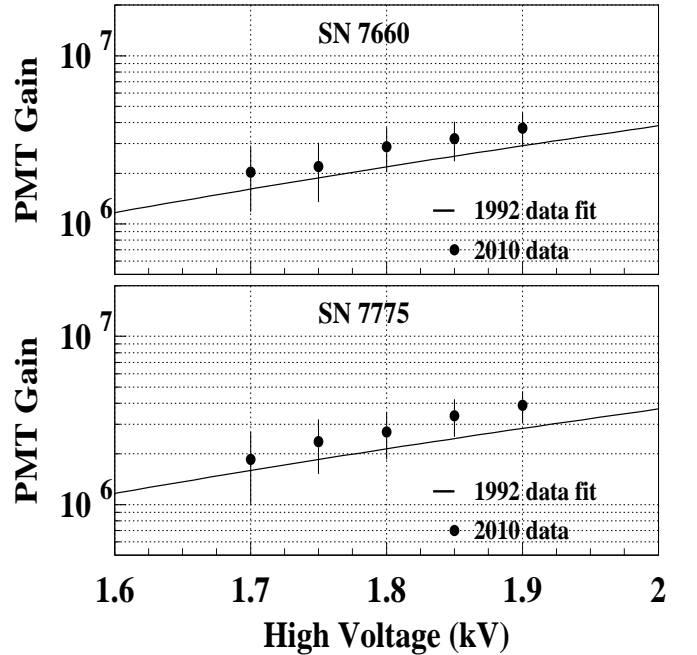

FIG. 25: Gain versus HV for two Photonis XP3462B PMTs. The lines are fits to the data from 1992 measurements. New measurements of 2010 are shown with solid symbols.
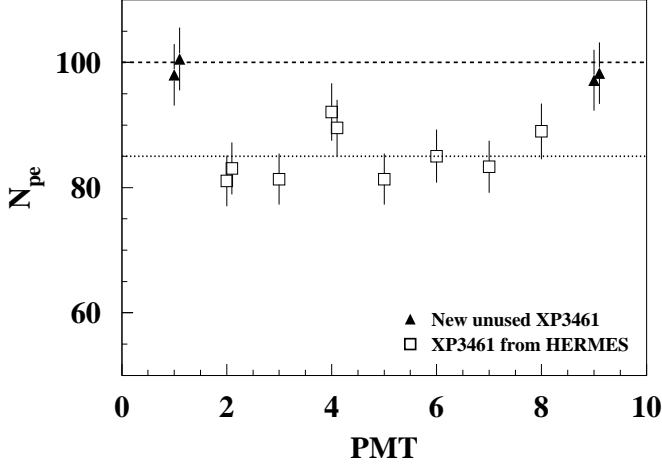
FIG. 26: Comparison of the detected number of photoelectrons at the gain 1.5×10^6 for the new XP3461 phototubes (triangle symbols), and for the PMTs taken from HERMES calorimeter (square symbols).
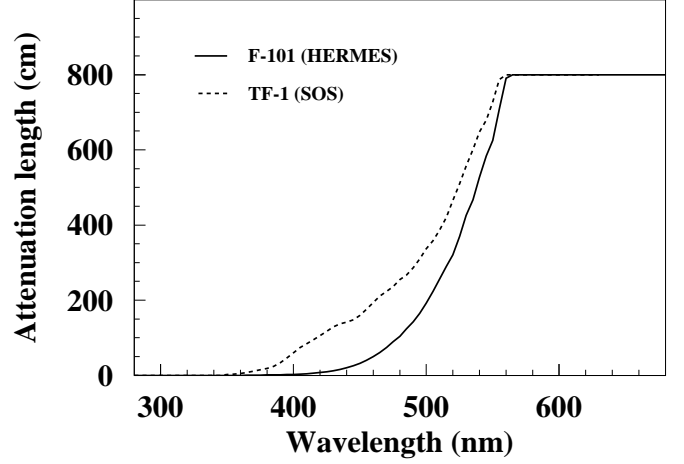

FIG. 27: Mean attenuation lengths of F-101 (solid line) and TF-1 (dotted line) lead-glasses used in the simulation of SHMS calorimeter. Data below 560 nm are extracted from transmittance measurements of the blocks. Above that the measurements are not reliable for the extraction, and the lengths are approximated by a large constant value.

tected photoelectrons will in this case be directly related with the quantum efficiencies of PMTs.

The comparison is shown in Fig. 26. A hint of aging, a 15% systematic decrease in quantum efficiency can be noticed. However, this is not taken into account in the simulations, for the decrease is marginal when compared to the accuracy of the measurements.

E. Simulation code for SHMS calorimeter

The code is based on GEANT4 simulation package [8], release 9.2. As in the simulations of the HMS calorimeter (see section III), the QGSP_BERT physics list was chosen to model hadron interactions. The code closely follows the parameters of the detector components mentioned in the previous sections. Other features are added into the model in order to bring it closer to reality as described below.

As optical measurements of both TF-1 and F-101 glasses revealed block to block variation in transparency, the attenuation lengths were randomly varied from block to block accordingly, around their mean values shown in Fig. 27. The quantum efficiencies of XP3462B and XP3461 PMT photocathodes are taken from the graphs provided by Photonis (see Fig. 4 and Fig. 22). The electronic effects in data acquisition system are taken into account assuming same performance as for the HMS calorimeter (see section III).

As in the HMS case, particles originate at the focal plane and traverse detector material and support structures in front of the calorimeter (see Table III). Note, the two SHMS aerogel detectors for kaon identification [53] are not considered here, since their design was not finalized by the time of the calculations. Focal plane coordinates, directions and deviations of momentum from

TABLE III: Materials between SHMS focal plane and calorimeter that are taken into account in the simulation. The listed positions are at the fronts of components

Component	Material	position (cm)	thickness (cm)	density (g/cm³)
DC2 gas	Ethane/Ar	40	3.81	0.00143
DC2 foils	Mylar		7×0.00254	1.4
S1X hodoscope	BC408 scint.	50	0.5	1.032
S1Y hodoscope	BC408 scint.	60	0.5	1.032
Gas Č gas	C_4F_8O	80	109.5	0.0089
Gas Č wind.	Al		2×0.1	2.6989
Gas Č mir.	glass		0.3	2.4
Gas Č mir.sup.	carbon fiber		0.1	1.8
S2X hodoscope	BC408 scint.	260	0.5	1.032
S2Y hodoscope	Quartz	265	2.5	2.634
Preshower sup.	Al	269	0.05	2.6989
Preshower cov.	Al	280	0.1	2.6989
Shower sup.	Al	282	0.05	2.6989

spectrometer setting were sampled by means of a Monte Carlo code of SHMS magnetic optics.

Light tracing is done within the frame of GEANT4 optics model. All the components related to the tracking of optical photons — like lead glass blocks, reflective foil wrapper, air layer between the reflector and the block, PMT glass windows, optical couplings of the windows and the blocks — were coded in terms of their sizes and optical parameters.

The calibration algorithm used in these studies is the same as for the HMS calorimeter (see subsection IV B): the variation of total energy deposition in Preshower and Shower relative to the energy of the primary electron
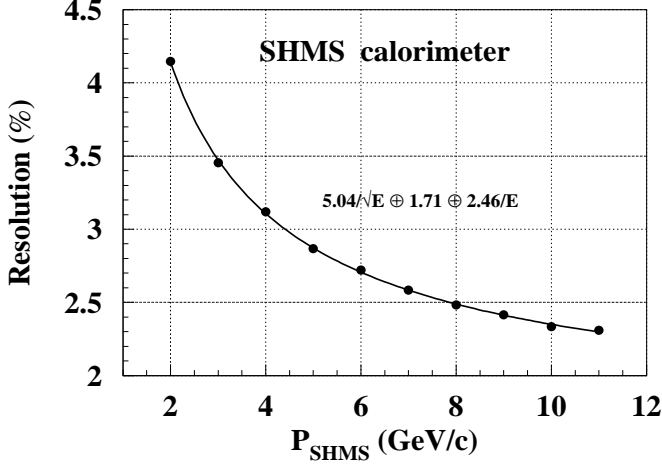
FIG. 28: Resolution of the modeled SHMS calorimeter. The small bullet symbols are data from the GEANT4 simulation, the line is the conventional 3-parameter fit [36] to them.

is minimized with respect to the calibration constants for each signal channel. The signals from Preshower are corrected for the horizontal coordinate of impact point. The signals from Shower are not corrected for impact point coordinates.

F.   Performance of SHMS calorimeter

Resolution of the modeled SHMS calorimeter (Fig. 28) is analogous to what has been reported for other lead-glass shower counters (references 21 through 31 in [54]), though it is somewhat lower compared to the HMS calorimeter (compare Fig. 28 with Fig. 15). Examination of the functional forms of energy dependencies of the two resolutions shows that the difference comes mainly from the stochastic term: compare $5.04\%\sqrt{E}$ for the SHMS with $3.75\%\sqrt{E}$ for the HMS. The stochastic term is sensitive to dead material before detector and to photoelectron statistics [36], which is in turn sensitive to the quality of radiator and light detectors. Both of these conditions are less favorable for the SHMS counter: there is more material between the focal plane and the calorimeter in the SHMS than in the HMS − ∼0.38 versus ∼0.16 radiation lengths respectively; and the lead-glass in SHMS calorimeter is less transparent than in the HMS calorimeter. The latter, combined with larger sizes, noticeably reduces photoelectron statistics in the SHMS calorimeter.

Despite that, decent electron/hadron separation can be achieved by using the signal from the Preshower in addition to the total energy deposition in the calorimeter. As an illustration of hadron/electron rejection capability, example histograms of energy depositions from e^- and π^- in the calorimeter and in the Preshower are presented in Fig. 29. As it is seen in the bottom panel, the minimum ionizing pions and the showering electrons are separable
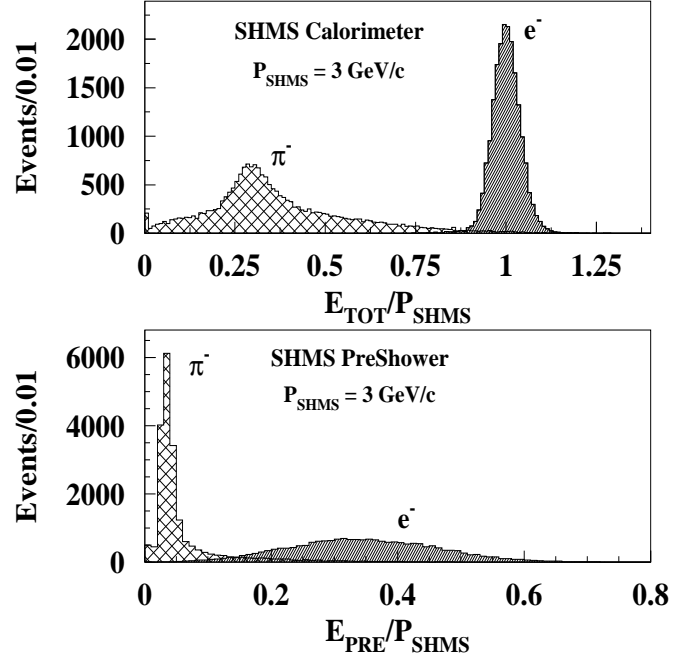

FIG. 29: Distribution of the normalized energy deposition from pions (hatched area) and electrons (full histogram) in SHMS calorimeter as a whole (top) and in Preshower only (bottom) at 3 GeV/c momentum setting.

to some extent in Preshower.

Electron detection efficiency and pion suppression factor for different cuts on the normalized total deposited energy are shown in Fig. 30 (compare with Fig. 16 and Fig. 18 for HMS calorimeter). For a constant cut, e^- detection improves with momentum, which is consistent with better resolutions at higher energies. Meanwhile, π^- rejection tends to worsen because of the increase in electromagnetic component of hadron induced cascades. The cut $E_{Dep}/P > 0.7$ ensures e^- detection better than 99.8% but modest π^- suppression of ∼10. By imposing higher cuts one can trade off e^- detection efficiency for a higher π^- suppression.

When compared to the HMS calorimeter, at the same cuts on total deposited energy the SHMS calorimeter ensures somewhat better e^- detection efficiency due to lower fraction of events of low visible energy deposition. Meanwhile, the π^- suppression is noticeably decreased (compare bottom panel in Fig. 30 with Fig. 18).

Calorimeter segmentation allows one to take advantage of the differences in the space development of electromagnetic and hadronic showers for PID. Electromagnetic showers develop earlier and deposit more energy at the start than hadronic cascades. Thus measuring energy deposited in the front layer of a detector along with total energy deposition improves the electron/hadron separation.

Pion suppression with the two PID methods − by using total energy deposition alone, and energy deposition
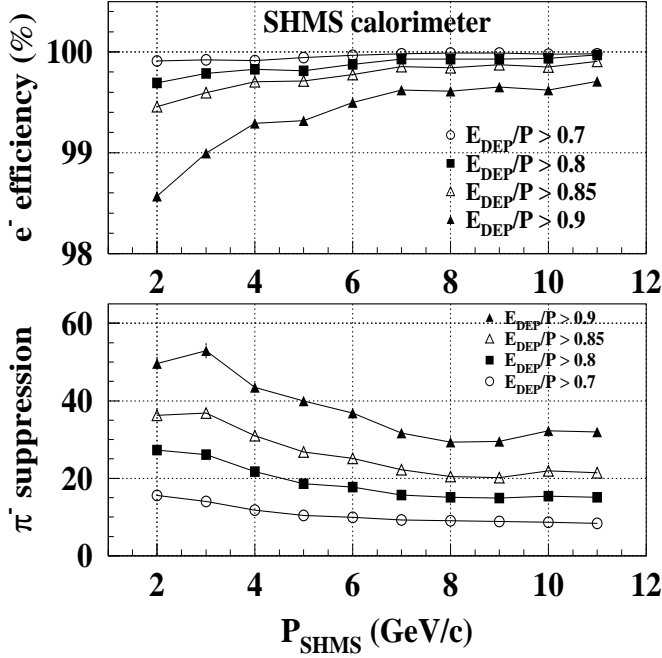
FIG. 30: Electron detection efficiency (top) and pion suppression factor (bottom) of the SHMS calorimeter versus spectrometer's momentum setting for different cuts on the normalized total energy deposition.
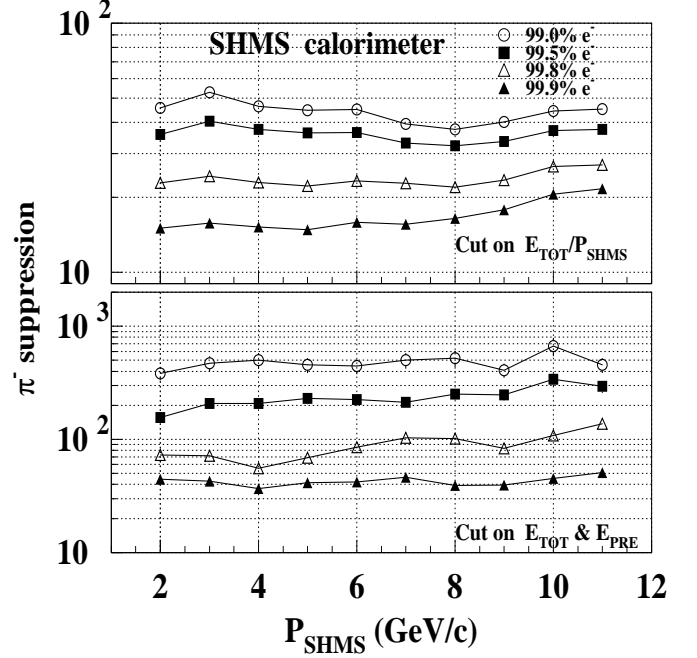

FIG. 31: Pion suppression factor versus SHMS momentum setting obtained with the two PID methods, for the different electron detection efficiencies indicated on the top panel. Data on the top panel are obtained by cutting on the normalized total energy deposition. Data on the bottom panel are obtained by applying two-dimensional cuts on the combination of total energy deposition and in the Preshower only.

in the Preshower together with total energy deposition − are compared in Fig. 31. Suppression factors on the top panel are obtained by imposing cuts on the total deposited energy. The cuts (shown in the top panel of Fig. 32) are chosen to ensure the electron detection efficiencies listed in the figures.

The suppression factors on the bottom panel are obtained by separation of pion and electron events of concurrent energy depositions in the Preshower and in the whole calorimeter (exemplified in the Fig. 32, bottom panel). The separation boundaries are tuned to the same electron detection efficiencies as in the first case, and are optimized for minimum error rate by means of SVM^{light} neural network [55]. Details can be found in a similar case with HMS calorimeter [54], where the forward layer of the counter was used as preshower. There, for the PID with combined energy depositions, from comparison with experimental data it was found that the simulation overestimates pion suppression, by ∼70% at low electron detection efficiencies $\gtrsim$90%, and ∼40% at high efficiencies ∼99.7%.

As it is seen in Fig. 31, in both cases there is a trend that suggests improvement of the π^- rejection with increase of momentum. Combining the total energy deposition E_{tot} with deposition in the Preshower E_{pre} significantly improves pion rejection. Gain in suppression by a factor of 2 - 10 times is achievable, dependent on momentum and the chosen e- efficiency. Generally the gain is bigger at higher momenta and for lower e^- detec-

tion efficiencies (see Fig. 33). Even for very high electron efficiencies, the combined cut yields a factor of two or more improvement in the pion rejection over the simple E_{TOT} cut. By using the Preshower the PID capabilities of the SHMS calorimeter become as good as that of HMS calorimeter where the first layer serves as Preshower.

To summarize results on the SHMS calorimeter, the GEANT4 simulations were conducted with realistic parameters of the detector. The simulations predict a resolution similar to other lead-glass counters, though somewhat worse than for the existing HMS calorimeter. Good electron/hadron separation can be achieved by using energy deposition in the Preshower along with total energy deposition in the calorimeter. In this case the PID capability is similar to the one attainable with the HMS calorimeter. A pion suppression factor of a few hundred is predicted at 99% electron efficiency.

VII. SUMMARY AND CONCLUSIONS

In summary, we have developed and constructed electromagnetic calorimeters from TF-1 type lead-glass blocks for the HMS and SOS magnetic spectrometers at JLab Hall C. The energy resolution better than $\sigma/E \sim 6\%/\sqrt{E}$ and the pion suppression ∼100:1 for ∼99% e^- detection efficiency have been achieved in the 1 – 5
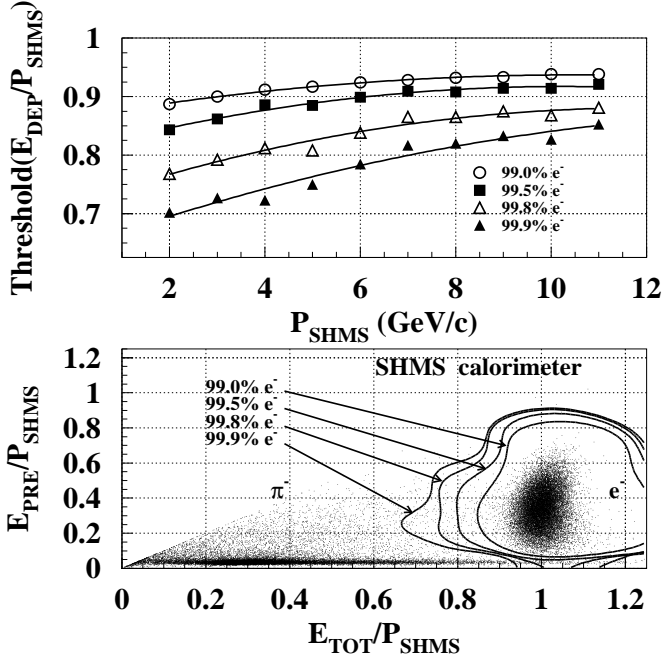
FIG. 32: Top: Cuts on the normalized total energy deposition for different e^- detection efficiencies. The quadratic fits to the data points have been used for evaluation of π^- suppression factors shown on the top panel of Fig. 31. Bottom: An example e^-/π^- separation by using combination of the normalized energy deposition in the calorimeter (Preshower+Shower) and Preshower at 3 GeV/c SHMS momentum setting. (In on-line electron events are in red, pion events are in blue). The loops are boundary for different e^- detection efficiencies, optimized by means of SVM neural network.
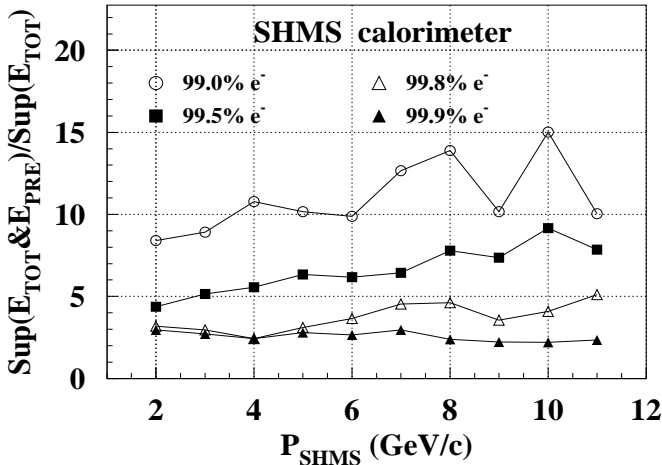
FIG. 33: Gain in π^- suppression from using energy deposition in Preshower along with total deposited energy in SHMS calorimeter.

GeV energy range. Performance of the HMS calorimeter within full momentum range of the spectrometer, attainable after CEBAF 12 GeV upgrade, is modeled by GEANT4 simulation. Within the limited momentum range the calculated resolution and π^- suppression factor are in good agreement with experimental data. The simulated pion suppression systematically exceeds experiment, by less than a factor of two, which is acceptable for rejection studies. The HMS/SOS calorimeters have been used in nearly all the Hall C experiments, providing good energy resolution and high pion suppression factor. No significant deterioration in the performance is observed in the course of operation since 1994.

Design construction of the electromagnetic calorimeter for the newly built SHMS spectrometer in Hall C has been finalized, based on extensive exploratory studies. From a few considered versions, the Preshower+Shower configuration was selected as most cost-effective. The Preshower will consist of a layer of 28 modules with TF-1 type lead glass radiators, stacked back to back in two columns. The Shower part will consist of 224 modules with F-101 type lead glass radiators, stacked in a "fly eye" configuration of 14 columns and 16 rows. 120×130 cm^2 of active area will cover beam envelope at the calorimeter.

A Monte Carlo program for the newly designed SHMS shower counter was developed, based on the GEANT4 simulation package, and simulations have been conducted with realistic parameters of the detector. The predicted resolution yields somewhat to the HMS calorimeter. Good electron/hadron separation can be achieved by using energy deposition in the Preshower along with total energy deposition in the calorimeter. In this case the PID capability is similar to or better than those attainable with HMS calorimeter. A pion suppression factor of a few hundreds is predicted for 99% electron detection efficiency.

[1] Conceptual Design Report (CDR). CEBAF Basic Experimental Equipment, CEBAF, Newport News, 1990.

[2] Conceptual Design Report (CDR) for The Science and Experimental Equipment for the 12 GeV upgrade of CEBAF, (Prepared for the DOE Science Review, April 6-8, 2005). Jefferson Lab, Newport News, March 25 2005.

[3] Measurement of the Charged Pion Form Factor to High Q^2. JLab proposal E12-06-101. G. M. Huber, D. Gaskell spokespersons.

[4] Lytcarino factory of optical glasses, 140061, Lytkarino, Moskow region, Russia.

[5] V.A. Davydov et al., Nucl. Instrum. Meth. 171 (1980) 465-467;

[6] T. Amatuni, G. Kazaryan, H. Mkrtchyan, V. Tadevosyan and W. Vulcan, Nucl. Instr. Meth. A 374, 39-47 (1996).

[7] W. R. Nelson, H. Hirayama, and D. W. O. Rogers, The EGS4 Code System, Report SLAC-265, Stanford Linear Accelerator Center, Stanford University, Stanford, California, 1985.

[8] S. Agostinelli et al., GEANT4–a simulation toolkit. Nucl. Instrum. Meth. A 506 (2003) 250-303; J. Allison et al., EEE Transactions on Nuclear Science 53, No.1, (2006) 270-278.

[9] C. Zorn, private communication.

[10] A. Gasparyan, H. Mkrtchyan, S. Wood, CEBAF 1992 Summer Workshop, AIP Conf. Proc. 269 (1992) 501-507.

[11] Photomultipliers, Philips, PC04.

[12] Ts. Amatuni, ELSS-1 Users Guide. Yerevan Physics Institute, Report EFI-760(75)-84, 1984.

[13] John Apostolakis et al., Progress in hadronic physics modeling in GEANT4. XIII Int. Conf. on Calorimetry in High Energy Physics. (CALO2008); J. of Phys. Conf. Series 160 (2009) 012073; J. Apostolakis et al., Hadronic Shower Shape Studies in GEANT4, CERN-LCGAPP-2007-02.

[14] http://geant4.cern.ch/support/proc-mod-catalog/physics-lists/useCases.shtml.

[15] G. Folger and J. P. Wellsch, String parton model in GEANT4, nucl-th/0306007; N. S. Amelin et al., Phys. Rev. Lett. 67 (1991) 1523.

[16] M. P. Guthrie, R. G. Alsmiller and H. W. Bertini, Nucl. Instrum. Meth. A 66 (1968) 29; Hugo W. Bertini, Phys.Rev. 188 (1969) 1715-1730.

[17] C. F. Powell, P. H. Fowler and D. H. Perkins, The study of elementary particles by photographic method. (Pergamon 1959); R. M. Brown et al., Phil. Mag. 40 (1949) 862.

[18] H. Fesefeldt, Report PITHA-85/02, RWTH Aachen (1985).

[19] http://www.sopra-sa.com

[20] M. Born, E. Wolf. Principles of Optics. Pergamon Press, 1965.

[21] T. Navasardyan et al., Phys. Rev. Lett. 98, 022001 (2007).

[22] J. Arrington, Inclusive Electron Scattering From Nuclei at $x > 1$ and High Q^2, PhD thesis, California Institute of Technology, 1998. Available from arXiv:nucl-ex/0608013.

[23] Ts. Amatuni, On the calibration of segmented full absorption calorimeters. Unpublished.

[24] T. Navasardyan, P. Bosted , M. Jones, HMS/SOS Tracking Code Enhancement, JLab note JLAB-PHY-06-482.

[25] V. Tvaskis, Longitudinal-Transverse Separation of Deep-Inelastic Scattering at Low Q^2 on Nucleons and Nuclei. PhD thesis, 2004, Vrije university.

[26] S. P. Malace et al, Phys.Rev. C 80, 035207 (2009).

[27] T. Horn et al. Phys. Rev. Lett. 97, 192001 (2006).

[28] M. I. Niculescu, Inclusive resonance electroproduction data from Hydrogen an Deuterium and studies of quark–hadron duality. PhD thesis, Hampton University 1999, unpublished.

[29] Jason Seely, Precise Measurement of the Nuclear Dependence of Structure Functions in Light Nuclei. PhD thesis, Massachusetts Institute of Technology, 2006, unpublished. Available from https://hallcweb.jlab.org/experiments/E03103/.

[30] Nadia Fomin, Inclusive electron scattering from nuclei in the quasielastic region at large momentum transfer. PhD thesis, Virginia State University, 2008. Available from arXiv:0812.2144.

[31] Aji Daniel, Precise measurement of the nuclear dependence of the EMC effect at large X. PhD thesis, Jefferson Lab, 2007, unpublished. Available from https://hallcweb.jlab.org/experiments/E03103/.

[32] Precision Measurement of the Nucleon Spin Structure Functions in the Region of Nucleon Resonances (RSS). JLab experiment E01-006. O. A. Rondon, S. Choi, M. Jones spokespersons.

[33] V. Mamyan, Measurements of F_2 and $R = \sigma_L/\sigma_T$ on Nuclear Targets in the Nucleon Resonance Region. PhD thesis, University of Virginia, 2010, unpublished.

[34] T. Navasardyan, Quark-Hadron Duality in Mesons Electroproduction. PhD thesis, Yerevan Physics Institute, 2007, unpublished.

[35] T. Horn, The Pion Charge Form Factor Through Pion Electroproduction, PhD thesis, University of Maryland, 2006, unpublished.

[36] C. Amsler et al. Particle Data Group, Phys. Lett. B 667, 1 (2008).

[37] H. Avakian et al., Nucl. Instrum. Meth. A 417 (1998) 69-78.

[38] L. Antoniazzi et al., Nucl. Instrum. Meth. A 332 (1993) 57-77.

[39] S. N. Maljukov et al., Characteristics of a Lead-Glass Electromagnetic Calorimeter in the WA91 Experiment. JINR preprint P1-95-283.

[40] C. Armstrong, Electroproduction of the $S_{11}(1535)$ Resonance at High Momentum Transfer, PhD thesis, College of William and Mary, 1998, unpublished.

[41] H. Avakian et al., Nucl. Instrum. Meth. A 378 (1996) 155-161.

[42] F. Binon et al., Nucl. Instrum. Meth. A 248 (1986) 86-102.

[43] A. Mkrtchyan, V. Tadevosyan, Monte Carlo Simulation

for SHMS Calorimeter Part I (Version 2a-2d). JLab note JLAB-TN-06-035.

[44] A. H. Mkrtchyan *et al.*, Monte Carlo Simulation for SHMS Calorimeter Part II. JLab note JLAB-TN-07-005.

[45] H. G. Mkrtchyan *et al.*, Electromagnetic Calorimeter for SHMS Spectrometer at JLab Hall C. National Academy of Sciences RA, El. J. of Natural Sciences, **1(14)**, 2010.

[46] J. Alcorn *et al.*, Nucl. Instrum. Meth. A **522** (2004) 294.

[47] M. Kobayashi *et al.*, Nucl. Instrum. Meth. A **345** (1994) 210-212.

[48] M. R. Adams *et al.*, Nucl. Instrum. Meth. A **238** (1985) 333.

[49] A. V. Inyakin *et al.*, Nucl. Instrum. Meth. **215** (1983) 103.

[50] M. Goldberg *et al.*, Nucl. Instrum. Meth. **108** (1973) 119.

[51] Arthur H. Mkrtchyan, Study of Radiation-induced optical effects on the lead-glass. National Academy of Sciences of RA, El. J. of Natural Sciences, physics, **1(16)** 2011.

[52] A. J. R. Puckett *et al.*, Phys. Rev. Lett. **104**, 242301 (2010).

[53] Studies of the L-T Separated Kaon Electroproduction Cross Section from 5-11 GeV. JLab proposal E12-09-011. T. Horn, G. M. Huber spokespersons.

[54] V. Tadevosyan, A. Asaturyan, A. Mkrtchyan, H. Mkrtchyan, S. Zhamkochyan, Monte Carlo Simulations of the JLab Hall C Calorimeters, Part I, HMS Calorimeter. JLab note JLAB-TN-10-016, 2010.

[55] http://svmlight.joachims.org/.